Computational 3-dimensional dislocation elastodynamics

Article *in* Journal of the Mechanics and Physics of Solids · February 2019

DOI: 10.1016/j.jmps.2019.02.008

Yinan Cui
Tsinghua University
31 PUBLICATIONS **281** CITATIONS

Giacomo Po
University of California, Los Angeles
65 PUBLICATIONS **502** CITATIONS

Yves-Patrick Pellegrini
Cea
50 PUBLICATIONS **520** CITATIONS

Markus Lazar
Technische Universität Darmstadt
113 PUBLICATIONS **1,829** CITATIONS

Computational 3-dimensional dislocation elastodynamics

Yinan Cui[a], Giacomo Po[a,b], Yves-Patrick Pellegrini[c], Markus Lazar[d], Nasr Ghoniem[a]

[a] *Department of Mechanical and Aerospace Engineering, University of California Los Angeles, Los Angeles, CA 90095*
[b] *Department of Mechanical and Aerospace Engineering, University of Miami, Coral Gables, FL 33146*
[c] *CEA, DAM, DIF, F-91297 Arpajon,France*
[d] *Department of Physics, Darmstadt University of Technology, Hochschulstr. 6, D-64289 Darmstadt, Germany*

Abstract

Understanding the mechanical behavior of solids at extremely high strain rates is of great scientific and technical interest. Current dislocation-based model of plasticity are typically implemented as quasi-static method. Their applicability to high strain rate condition is limited, because the influence of the elastodynamic stress field at extreme strain rates on the collective behavior of 3-dimensional (3D) dislocations is not clear, and the time-dependent nature is very important when the strain rate is higher than $10^6 \mathrm{s}^{-1}$ (e.g. laser shock loading). To overcome this limitation, we present here the first computational procedure for 3D discrete dislocation elastodynamics (DDE). A novel computational method is developed for calculations of the fully-resolved elastodynamic field of non-uniformly moving dislocation loops. The developed method here extends the technique of retarded potentials, which was originally used to describe the electrodynamics of charged particles moving near the speed of light. Comparison with independent 2D calculations establish the accuracy and convergence of the numerical scheme. It is shown that dislocation loop motion near the sound speed results in significant restructuring of the emitted elastodynamic fields. New insights on short-time dislocation interactions during shock loading are also revealed through a study of the forces between rapidly-moving shear dislocation loops.

Keywords: Dislocation dynamics, elastodynamics, shock loading, high strain rate.

Contents

1 Introduction **3**

2 Elastodynamic Field of Non-uniformly Moving Dislocation Loop **4**
- 2.1 The 3D Elastodynamic Problem 4
- 2.2 The Elastodynamic Field of a Non-uniformly Moving Dislocation Loop 6

3 Numerical Implementation in 3D-DDE **9**
- 3.1 Dislocation Motion History 9
- 3.2 Determination of Retarded Times & Positions 11
- 3.3 Fast Sum Implementation of Line Integrals 13
- 3.4 Computation of Time Derivatives 14
- 3.5 Singularity Treatment 15

4 Validation tests **17**
- 4.1 Determination of the Retarded Dislocation Segment 17
- 4.2 The Injected Static Edge Dislocation 17
- 4.3 Uniform Motion of a Straight Edge Dislocation 21
- 4.4 Motion of a Straight Screw Dislocation 22

Email address: `cuiyinan@ucla.edu` (Yinan Cui)

Preprint submitted to Journal of the Mechanics and Physics of Solids,https://doi.org/10.1016/j.jmps.2019.02.008 *February 11, 2019*

5 New Insights on Elastodynamic Effects **23**
5.1 Stress field of a moving shear dislocation loop 23
5.2 Interaction between shear dislocation loops 29

6 Conclusions **31**

1. Introduction

The elastic field of dislocations in materials under shock loading is of general interest, both from a fundamental perspective and in many applications. These encompass a wide range from small scale laser, electron or ion interaction with materials, to the large scale of earthquakes (Gurrutxaga-Lerma et al., 2015a; Luscher et al., 2017; Ni and Markenscoff, 2016; Yanilkin et al., 2014). Several interesting observations, for example, have been made during the past few decades, where the elastic field of high-speed dislocations plays a decisive role. In extreme compression experiments, the launched shock wave nucleates dislocations at its front, with the elastic wave preceding the dislocation nucleation zone. The interaction between the elastic wave and the elasto-dynamic field of dislocations has been shown to explain the decay of the elastic wave precursor (Gurrutxaga-Lerma et al., 2015a). Superposition of solutions for dislocations activated by an incident plane wave was used to determine the decay of the wave amplitude (Clifton and Markenscoff, 1981; Markenscoff and Clifton, 1981).

A fundamental understanding of dynamic plasticity in materials under shock loading is yet to emerge, despite the many decades of experimental observations and more recent modeling (Shehadeh and Zbib, 2016; Xiong et al., 2016). One of the main reasons is the difficulty in the precise determination of the elastodynamic stress field of 3D dislocations. Without this basic ingredient, it is difficult, if not impossible, to explain many observed phenomena of materials loaded at extreme strain rates. The experimentally observed microstructure is clearly distinguished from what is seen in materials loaded at low strain rates. For example, copious concentrations of *dislocation debris* is often observed at high strain rates (Bringa et al., 2005; Lu et al., 2005), and the exact mechanism is not understood. Moreover, competition between dislocation-dominated plasticity and a twinning mode of deformation is shown to lead to a transition at high strain rates (Meyers, 1994; Pang et al., 2018). In addition, micro-shear bands are known to be favored at high strain rates as a result of dislocation channeling and plastic flow localization (Longère and Dragon, 2015; Meyers, 1994). The intense heating in these zones can lead to premature recrystallization as the strain rate is increased (Cao et al., 2005). Among all these features, the contribution of the elastodynamic field induced by high speed dislocations is not clear.

Generally, stress waves emanating from a moving dislocation travel at the transverse/longitudinal sound speed, in the order of 1 km/s. If the dislocation velocity is also in the order of sound speed, the spatial and temporal structure of stress waves, to a stationary observer in the material, are expected to be strongly influenced by the moving dislocation source speed. Consider, for example, the case of laser shock loading where the plastic strain rate $\dot{\varepsilon}^{\mathrm{P}}$ is well above $10^6 \mathrm{s}^{-1}$. According to Orowan's equation $\dot{\varepsilon}^{\mathrm{P}} = \rho b v$, where ρ is the mobile dislocation density, assumed to be in the order of $10^{13} \mathrm{m}^{-2}$, b is the magnitude of Burger's vector (≈ 0.25 nm), and v is the average dislocation velocity. Thus, for a strain rate above $2.5 \times 10^6 \mathrm{s}^{-1}$, the dislocation speed is expected to be above 1 km/s. Thus, for such high strain rates induced by lasers, ions or electrons, the elastodynamic stress field of the dislocation is expected to be significantly different from its quasi-static counterpart.

Nevertheless, as a result of the complicated equations for fully-resolved elastodynamics, the stress field of high speed dislocations is generally approximated by their static solution. For such an approximation, the stress field of a moving dislocation is assumed to instantaneously span the entire domain, regardless of its extent. Dislocations moving behind a shock front will artificially change the stress field ahead of the front (Pillon and Denoual, 2009). This is found to trigger spurious dislocation nucleation ahead of the shock front (Gurrutxaga-Lerma et al., 2013), which is obviously unphysical. This is not surprising since the elastodynamic stress field has been recognized to be significantly different from the static stress field of dislocations since the mid twentieth century (Eshelby, 1949; Frank, 1949; Lazar, 2013b; Markenscoff and Clifton, 1981; Mura, 1963; Pellegrini and Lazar, 2015). The simplest example is the field of an infinitely-long screw dislocation with uniform velocity, which exhibits the so called "relativistic" effect. When the velocity approaches the transverse wave speed, the field behavior is similar to Einstein's theory of relativity for particles approaching the speed of light (Hirth and Lothe, 1982). The displacement field expression of the uniformly moving screw dislocation is found to be the same as the static solution, apart from a "Lorentz contraction". With the increase of its velocity, the corresponding isostress contours are gradually compressed along the moving direction. We note here that while the speed of light is an upper limit in the theory of relativity, a supersonic dislocation can move faster than the transverse wave speed (c_{T}) (Eshelby, 1956; Gumbsch and Gao, 1999; Nosenko et al., 2007). Lazar et al. derived expressions for the nonsingular subsonic and supersonic solutions of the elastic fields and the dislocation density tensor for a screw dislocation. Both the dislocation density tensor and the stress field exhibits a Mach cone for supersonic motion (Lazar, 2009; Lazar and Pellegrini, 2016). As a natural outcome of the strongly different stress field map induced by this purely elastodynamic effect, the fundamental dislocation interaction and their self force under shock loading are expected to behave differently from conventional static case (Pellegrini, 2014). For example, the interaction force between two coplanar moving screw dislocations decreases with the increase in their uniform velocity. Recent molecular dynamics simulations demonstrate that when two oppositely signed, coplanar edge dislocations glide towards one another at speeds close to or exceeding the transverse wave speed, they may "overshoot" one another, or "rebound" etc, instead of annihilation, because the contribution of the kinetic energy associated with the high speed dislocation overcomes the effect of the stationary potential energy described by conventional Frank's rule (Chu et al., 2012; Li et al., 2016). Obviously, using a static field solution will not be able to capture these abnormal dynamic effects.

The vast majority of information concerning elastodynamic effects on fundamental dislocation behavior has been obtained either from experiments (Meyers, 1994; Nosenko et al., 2007), theoretical analysis (Callias et al., 1990; Lazar and Pellegrini, 2016; Markenscoff, 2010; Meyers, 1994; Pellegrini and Lazar, 2015), or molecular dynamics simulations (Bringa et al., 2006; Chu et al., 2012; Colorado et al., 2013; Gumbsch and Gao, 1999; Jiang et al., 2012; Li et al., 2016; Seif et al., 2014; Wang and Beyerlein, 2008; Youssef et al., 2013). These pioneering efforts lead to numerous new insights. However, theoretical studies are mainly limited to simple configurations, while MD calculations are restricted by the simulation time and spatial scales. Only recently, a concurrent atomistic-continuum methodology (Xiong et al., 2016) was developed, which quantifies the elastodynamic effects by coarse-graining two dimensional (2D) atomistic calculations. On the other hand, the elastodynamic stress field has been recently considered in 2D discrete dislocation dynamics (DDD) simulations (Gurrutxaga-Lerma et al., 2013, 2015a; Pellegrini and Lazar, 2015), which captures the full time- and history-dependent nature of the behavior of pure edge dislocations. However, the key approximations inherent in 2D techniques do not allow a clear insight into the influence of elastodynamics on 3D-dislocations. This is particularly true when one is interested in the outcome of short-range and long-range interactions between 3D dislocations. Till now, in all the available 3D-DDD methods, the elastodynamic solution is never directly considered. One main pioneering development is introducing an inertia term in the kinetic equation to consider energy radiation from an accelerating dislocation (Hu et al., 2017; Liu et al., 2008; Shehadeh et al., 2005; Shehadeh and Zbib, 2016). Nonetheless, the static dislocation stress solution is widely used. 3D-DDD simulations based on the full elastodynamics framework have not yet been attempted, which considerably restricts a complete fundamental understanding of the elastodynamics effects on micro-scale plasticity.

To fill this gap, we develop a new computational method that enables full 3D discrete dislocation elastodynamics (DDE) computer simulations. The technique we pursue here is based on the retarded-time method, developed within the framework of classical electrodynamics with the Liénard-Wiechert retarded potentials (Lazar, 2013b). One important advantage of this approach is that the computational method is consistent with current 3D DDD simulation codes, and will thus enable their extension to studies of shock physics. To achieve this challenging goal, several issues must be resolved. First, the elastodynamics solution for the nonuniform motion of 3D dislocations is not complete, although several important contributions have been made (Lazar and Pellegrini, 2016; Markenscoff and Clifton, 1981; Mura, 1963) and their elastic distortion solution is given (Lazar, 2013b). Till now, there is no explicit compact formula of the elastodynamics stress field of high speed 3D dislocations with non-uniform motion, which can be directly used for numerical implementation. Second, the numerical implementation of the fully elastodynamic solution is an unexplored problem to date in 3D-DDE simulations. For example, an effective method must be proposed to record and deal with the full history of dislocation motion. The singularity related with the dislocation core and the wave front must be correctly treated. Finally, one needs to understand computer simulation results, going beyond complicated equations, so as to extract physical insight. To shed light on these questions, we present details of the numerical method in sections 2-4. Then, in section 5, we aim to apply the developed numerical scheme to several unexplored interesting problems. A shear dislocation loop is taken as an example to reveal the specific nature and influence of the temporal evolution of the elastic field on the outcome of subsequent interactions. Concluding remarks are given in section 6, together with a discussion on potential future efforts that will be enabled by the current development.

2. Elastodynamic Field of Non-uniformly Moving Dislocation Loop

2.1. The 3D Elastodynamic Problem

We derive here the fundamental equations of 3D elastodynamics, with the main objective being the ability to calculate the elastic field of a non-uniformly moving dislocation loop as a result of its eigendistortion. The derivation is an extension of earlier work by Mura (1963), Callias et al. (1990); Markenscoff and Clifton (1981), and Lazar (2013b). We wish here to obtain a compact formula and establish a numerical way to calculate the elastodyanamic field. The equilibrium equation is given by:

$$\sigma_{ij,j} + f_i = \rho \ddot{u}_i \tag{1}$$

where σ is the stress tensor, f is body force density vector, ρ is material density, and u is displacement vector. $()_{,i}$ denotes differentiation with respect to x_i, and a superposed dot means a time derivative. Assuming that displacement gradient is split into an elastic distortion β^{E}_{ij} and a plastic distortion part β^{P}_{ij},

$$u_{i,j} = \beta^{\mathrm{E}}_{ij} + \beta^{\mathrm{P}}_{ij}. \tag{2}$$

Thus, the constitutive relation can be expressed as

$$\sigma_{ij} = C_{ijkl}\beta^{\mathrm{E}}_{kl}. \tag{3}$$

where C_{ijkl} is elastic modulus tensor.

Upon substituting Eq. (2) and Eq. (3) into Eq. (1), we have

$$C_{ijkl}(u_{k,lj} - \beta^{\mathrm{P}}_{kl,j}) + f_i = \rho \ddot{u}_i, \tag{4a}$$

$$(C_{ijkl}\partial_l\partial_j - \rho\delta_{ik}\partial_t\partial_t)u_k = C_{ijkl}\beta^{\mathrm{P}}_{kl,j} - f_i, \tag{4b}$$

where ∂_t means differentiation with respect to time t. We define the differential operator L_{ik} as follows [1]:

$$L_{ik} = C_{ijkl}\partial_l\partial_j - \rho\delta_{ki}\partial_t\partial_t. \tag{5}$$

The dynamic Green tensor G_{km} corresponding to L_{ik} meets the following condition:

$$L_{ik}G_{km} = \delta_{im}\delta(t)\delta(\mathbf{x}), \tag{6}$$

where $\delta()$ is the Dirac delta function, and δ_{im} is the Kronecker delta. $\mathbf{x}$ is a position vector of the source point. Thus, the displacement vector field can be obtained by the spatio-temporal convolution between G_{km} and the source term in Eq. (4b). If one ignores body force f,

$$u_k = G_{km} * C_{mnpq}\beta^{\mathrm{P}}_{pq,n}, \tag{7}$$

where $*$ represents a convolution integral. Note that Eq. (7) is applicable to unbounded media, and is based on the assumption of zero initial velocity, which means that β^{E}_{ij} and β^{P}_{ij} and their first time derivatives are zero for $t_0 \to -\infty$ (Anderson, 1992). This zero initial velocity condition assumption includes the case of a dislocation at rest, which may have started moving at time $t_0 \neq -\infty$, so the initial static field is part of the solution (Callias et al., 1990). Initial conditions are discussed in section 2.2 in (Lazar and Pellegrini, 2016). Following the Mura-Wills procedure, the displacement gradient tensor $u_{k,l}$ is therefore,

$$\begin{aligned} u_{k,l} &= G_{km} * C_{mnpq}\beta^{\mathrm{P}}_{pq,nl} = C_{mnpq}G_{km,n} * (\beta^{\mathrm{P}}_{pl,q} + \epsilon_{rql}\alpha_{pr}) = C_{mnpq}G_{km,nq} * \beta^{\mathrm{P}}_{pl} + C_{mnpq}G_{km,n} * (\epsilon_{rql}\alpha_{pr}) \\ &= (L_{mp} + \rho\delta_{mp}\partial_t\partial_t)G_{km} * \beta^{\mathrm{P}}_{pl} + C_{mnpq}\epsilon_{rql}G_{km,n} * \alpha_{pr} = \beta^{\mathrm{P}}_{kl} + \rho\dot{G}_{kp} * \dot{\beta}^{\mathrm{P}}_{pl} + C_{mnpq}\epsilon_{rql}G_{km,n} * \alpha_{pr}, \end{aligned} \tag{8}$$

where $\alpha_{pr} = \epsilon_{rhs}\beta^{\mathrm{P}}_{ph,s}$. According to Eq. (8) and Eq. (2), it is easy to find an expression for the elastic distortion,

$$\beta^{\mathrm{E}}_{kl} = \rho\dot{G}_{kp} * \dot{\beta}^{\mathrm{P}}_{pl} + C_{mnpq}\epsilon_{rql}G_{km,n} * \alpha_{pr}. \tag{9}$$

---

[1] Expressions in previous work mainly contain a negative sign. Here, we write the expression to be directly consistent with the static case. Note that this treatment also leads to a different sign of the Green tensor, compared with previous work.

Combining Eq. (9) and Eq. (3),

$$\sigma_{ij} = \rho C_{ijkl}\dot{G}_{kp} * \dot{\beta}^{\mathrm{P}}_{pl} + C_{ijkl}C_{mnpq}\epsilon_{rql}G_{km,n} * \alpha_{pr}. \tag{10}$$

The derivations above apply to both anisotropic and isotropic materials. Considering that it is easier to obtain the Green's function in isotropic crystals, only the isotropic case is considered from this point forward. Here, the elastic modulus tensor has the special form: $C_{ijkl} = \lambda\delta_{ij}\delta_{kl} + \mu(\delta_{ik}\delta_{jl} + \delta_{il}\delta_{jk})$, where λ and μ are Lamé's first parameter and shear modulus, respectively. The elastodynamic Green's function in an isotropic crystal is derived in (Achenbach, 2003; Eringen et al., 1977)

$$G_{ij}(\mathbf{x}, t) = \frac{-1}{4\pi\rho x}\left\{\frac{1}{c_{\mathrm{T}}^2}\left(\delta_{ij} - \frac{x_i x_j}{x^2}\right)\delta\left(t - \frac{x}{c_{\mathrm{T}}}\right) + \frac{1}{c_{\mathrm{L}}^2}\frac{x_i x_j}{x^2}\delta\left(t - \frac{x}{c_{\mathrm{L}}}\right) + \left(\frac{3x_i x_j}{x^2} - \delta_{ij}\right)\frac{1}{x^2}\int_{x/c_{\mathrm{L}}}^{x/c_{\mathrm{T}}} \tau\delta\left(t - \tau\right)\mathrm{d}\tau\right\}, \tag{11}$$

where $c_{\mathrm{T}} = \sqrt{\mu/\rho}$, and $c_{\mathrm{L}} = \sqrt{(2\mu + \lambda)/\rho}$ are the velocities of the transverse and longitudinal elastic waves, respectively. x and x_i is the magnitude and the ith component of position vector $\mathbf{x}$, respectively. The three main terms in the big bracket of Eq. (11) represent a far-field transverse wave components, a far-field longitudinal wave component, and a near-field mixed wave component, respectively. The reader interested into more detailed discussions on the properties of Eq. (11) is referred to chapter 9 of reference (Pujol, 2003).

The spatial and time derivatives of the elastodynamic Green's function, needed to determine the stress field in Eq. (10), are given by (see Appendix A for derivation details),

$$\begin{aligned}
G_{ij,k}(\mathbf{x}, t) \quad = \quad & \frac{-1}{4\pi\rho}\left\{\frac{1}{c_{\mathrm{T}}^2}\left(-\frac{2\delta_{ij}x_k + \delta_{ik}x_j + \delta_{jk}x_i}{x^3} + \frac{6x_i x_j x_k}{x^5}\right)\delta\left(t - \frac{x}{c_{\mathrm{T}}}\right) - \frac{x_k}{c_{\mathrm{T}}^3 x^2}\left(\delta_{ij} - \frac{x_i x_j}{x^2}\right)\partial_t\left(\delta\left(t - \frac{x}{c_{\mathrm{T}}}\right)\right)\right. \\
& + \frac{1}{c_{\mathrm{L}}^2}\left(\frac{\delta_{ik}x_j + \delta_{jk}x_i + \delta_{ij}x_k}{x^3} - \frac{6x_i x_j x_k}{x^5}\right)\delta(t - \frac{x}{c_{\mathrm{L}}}) - \frac{1}{c_{\mathrm{L}}^3}\frac{x_i x_j x_k}{x^4}\partial_t\left(\delta(t - \frac{x}{c_{\mathrm{L}}})\right) \\
& \left. + \left(\frac{3\delta_{ij}x_k + 3\delta_{jk}x_i + 3\delta_{ik}x_j}{x^5} - \frac{15x_i x_j x_k}{x^7}\right)\int_{x/c_{\mathrm{L}}}^{x/c_{\mathrm{T}}} \tau\delta\left(t - \tau\right)\mathrm{d}\tau\right\}, \qquad (12) \\
\dot{G}_{ij}(\mathbf{x}, t) \quad = \quad & \frac{-1}{4\pi\rho x}\left\{\frac{1}{c_{\mathrm{T}}^2}\left(\delta_{ij} - \frac{x_i x_j}{x^2}\right)\partial_t\left(\delta\left(t - \frac{x}{c_{\mathrm{T}}}\right)\right) + \frac{1}{c_{\mathrm{L}}^2}\frac{x_i x_j}{x^2}\partial_t\left(\delta\left(t - \frac{x}{c_{\mathrm{L}}}\right)\right) + \right. \\
& \left.\left(\frac{3x_i x_j}{x^2} - \delta_{ij}\right)\frac{1}{x^2}\left(\int_{x/c_{\mathrm{L}}}^{x/c_{\mathrm{T}}} \delta\left(t - \tau\right)\mathrm{d}\tau + \frac{x}{c_{\mathrm{L}}}\delta\left(t - \frac{x}{c_{\mathrm{L}}}\right) - \frac{x}{c_{\mathrm{T}}}\delta\left(t - \frac{x}{c_{\mathrm{T}}}\right)\right)\right\}. \qquad (13)
\end{aligned}$$

Derivatives of the Green's function developed above can be readily used to obtain the stress field induced by an arbitrary eigendistorsion β^{P}. In addition, it is easy to obtain the static stress field $\sigma_{ij} = C_{ijkl}C_{mnpq}\epsilon_{rql}G_{km,n} * \alpha_{pr}$, if we omit the time derivative terms in Eq. (10). The resulting static solution is consistent with Eq. (18) in reference (Po et al., 2018).

2.2. The Elastodynamic Field of a Non-uniformly Moving Dislocation Loop

In this section, the eigendistorsion induced by a non-uniformly moving dislocation loop will be considered as a specific example, to derive the corresponding elastodynamics stress field. Assuming that a dislocation loop with Burger's vector $\mathbf{b}$ expands over a surface S with slip area A, the corresponding plastic distortion is expressed as follows (Lazar, 2013b; Mura, 1963; Po et al., 2018):

$$\beta^{\mathrm{P}}_{ph}(\mathbf{x}, t) = -\int_{S(t)} \delta(\mathbf{x} - \mathbf{s}')b_p dA'_h, \tag{14}$$

where $\mathbf{s}'$ is the integration point position at time t and b is Burger's vector. According to stokes' theorem, the dislocation density tensor $\boldsymbol{\alpha}$ turns out to be concentrated on the dislocation line, which is $\mathcal{L} = \partial S$, bounding the surface S.

$$\alpha_{pr}(\mathbf{x}, t) = \epsilon_{rhs}\beta^{\mathrm{P}}_{ph,s} = \oint_{\mathcal{L}(t)} \delta(\mathbf{x} - \mathbf{s}')b_p\xi_r \mathrm{d}L', \tag{15}$$

where ξ is the unit tangent direction vector of dislocation line. The plastic distortion rate induced by the moving dislocation can be obtained according to Orowan's relation,

$$\dot{\beta}^{\mathrm{P}}_{pl}(\mathbf{x}, t) = -\oint_{\mathcal{L}(t)} \delta(\mathbf{x} - \mathbf{s}') b_p \epsilon_{lsr} V_s \xi_r \mathrm{d}L', \tag{16}$$

where $V = \dot{\mathbf{s}}'$ is the dislocation velocity vector at any integration point $\mathbf{s}'$ on the dislocation loop.

Substituting Eq. (15), and Eq. (16) into Eq. (9), the elastodynamic elastic distortion induced by the dislocation loop is (see also (Markenscoff, 1983)),

$$\begin{aligned}\beta^{\mathrm{E}}_{kl}(\mathbf{x}, t) = &\int_{t_0}^{t} \mathrm{d}t' \oint_{\mathcal{L}(t')} \epsilon_{rql} C_{mnpq} G_{km,n}(\mathbf{x} - \mathbf{s}', t - t') b_p \xi_r(\mathbf{s}', t') \mathrm{d}L' \\ &- \int_{t_0}^{t} \mathrm{d}t' \oint_{\mathcal{L}(t')} \rho \dot{G}_{kp}(\mathbf{x} - \mathbf{s}', t - t') b_p \epsilon_{lsr} V_s(\mathbf{s}', t') \xi_r(\mathbf{s}', t') \mathrm{d}L'.\end{aligned} \tag{17}$$

Upon substitution of Eqs. (12) and (13) into Eq. (17), the retarded solution is obtained by firstly performing temporal integration with $\delta(t - t' - \frac{x - x'}{c})$ terms in the Green's function,

$$\begin{aligned}\boldsymbol{\beta}^{\mathrm{E}}(\mathbf{x}, t) = -\frac{1}{4\pi}\Bigg\{ &\oint_{\mathcal{L}(t-R/c_{\mathrm{T}})} \frac{1}{R^2(R - \mathbf{R}\cdot\mathbf{V}/c_{\mathrm{T}})} \left(3\mathbf{b}\otimes(\mathbf{R}\times\boldsymbol{\xi}) + 3(\mathbf{b}\cdot\mathbf{R})\,\boldsymbol{\Xi} + 2\mathbf{R}\otimes(\mathbf{b}\times\boldsymbol{\xi}) - 12\frac{\mathbf{R}\otimes(\mathbf{R}\times\boldsymbol{\xi})(\mathbf{b}\cdot\mathbf{R})}{R^2}\right)\mathrm{d}L' \\ +\partial_t &\oint_{\mathcal{L}(t-R/c_{\mathrm{T}})} \frac{1}{c_{\mathrm{T}}R(R - \mathbf{R}\cdot\mathbf{V}/c_{\mathrm{T}})} \left(\mathbf{b}\otimes(\mathbf{R}\times\boldsymbol{\xi}) + (\mathbf{b}\cdot\mathbf{R})\,\boldsymbol{\Xi} - 2\frac{\mathbf{R}\otimes(\mathbf{R}\times\boldsymbol{\xi})(\mathbf{b}\cdot\mathbf{R})}{R^2}\right)\mathrm{d}L' \\ + &\oint_{\mathcal{L}(t-R/c_{\mathrm{L}})} \frac{(1-2\nu)/(1-\nu)}{R^2(R - \mathbf{R}\cdot\mathbf{V}/c_{\mathrm{L}})} \left(\frac{3\nu-1}{1-2\nu}\mathbf{R}\otimes(\mathbf{b}\times\boldsymbol{\xi}) - \mathbf{b}\otimes(\mathbf{R}\times\boldsymbol{\xi}) - (\mathbf{b}\cdot\mathbf{R})\,\boldsymbol{\Xi} + 6\frac{\mathbf{R}\otimes(\mathbf{R}\times\boldsymbol{\xi})(\mathbf{b}\cdot\mathbf{R})}{R^2}\right)\mathrm{d}L' \\ +\partial_t &\oint_{\mathcal{L}(t-R/c_{\mathrm{L}})} \frac{(1-2\nu)/(1-\nu)}{c_{\mathrm{L}}R(R - \mathbf{R}\cdot\mathbf{V}/c_{\mathrm{L}})} \left(\frac{\nu}{1-2\nu}\mathbf{R}\otimes(\mathbf{b}\times\boldsymbol{\xi}) + \frac{\mathbf{R}\otimes(\mathbf{R}\times\boldsymbol{\xi})(\mathbf{b}\cdot\mathbf{R})}{R^2}\right)\mathrm{d}L' \\ + &\int_{1/c_{\mathrm{L}}}^{1/c_{\mathrm{T}}} \oint_{\mathcal{L}(t-\kappa R)} \frac{6c_{\mathrm{T}}^2\kappa}{R^2(R - \kappa\mathbf{R}\cdot\mathbf{V})} \left(-\mathbf{b}\otimes(\mathbf{R}\times\boldsymbol{\xi}) - (\mathbf{b}\cdot\mathbf{R})\,\boldsymbol{\Xi} - \mathbf{R}\otimes(\mathbf{b}\times\boldsymbol{\xi}) + 5\frac{\mathbf{R}\otimes(\mathbf{R}\times\boldsymbol{\xi})(\mathbf{b}\cdot\mathbf{R})}{R^2}\right)\mathrm{d}L'\,\mathrm{d}\kappa \\ +\partial_t &\oint_{\mathcal{L}(t-R/c_{\mathrm{T}})} \frac{1}{c_{\mathrm{T}}^2(R - \mathbf{R}\cdot\mathbf{V}/c_{\mathrm{T}})} \left(-\mathbf{b}\otimes(\mathbf{V}\times\boldsymbol{\xi}) + \frac{\mathbf{R}\otimes(\mathbf{V}\times\boldsymbol{\xi})(\mathbf{b}\cdot\mathbf{R})}{R^2}\right)\mathrm{d}L' \\ -\partial_t &\oint_{\mathcal{L}(t-R/c_{\mathrm{L}})} \frac{1}{c_{\mathrm{L}}^2(R - \mathbf{R}\cdot\mathbf{V}/c_{\mathrm{L}})} \frac{\mathbf{R}\otimes(\mathbf{V}\times\boldsymbol{\xi})(\mathbf{b}\cdot\mathbf{R})}{R^2}\,\mathrm{d}L' \\ + &\int_{1/c_{\mathrm{L}}}^{1/c_{\mathrm{T}}} \oint_{\mathcal{L}(t-\kappa R)} \frac{1}{R(R - \kappa\mathbf{R}\cdot\mathbf{V})} \left(\mathbf{b}\otimes(\mathbf{V}\times\boldsymbol{\xi}) - 3\frac{\mathbf{R}\otimes(\mathbf{V}\times\boldsymbol{\xi})(\mathbf{b}\cdot\mathbf{R})}{R^2}\right)\mathrm{d}L'\,\mathrm{d}\kappa \\ - &\oint_{\mathcal{L}(t-R/c_{\mathrm{T}})} \frac{1}{c_{\mathrm{T}}R(R - \mathbf{R}\cdot\mathbf{V}/c_{\mathrm{T}})} \left(\mathbf{b}\otimes(\mathbf{V}\times\boldsymbol{\xi}) - 3\frac{\mathbf{R}\otimes(\mathbf{V}\times\boldsymbol{\xi})(\mathbf{b}\cdot\mathbf{R})}{R^2}\right)\mathrm{d}L' \\ + &\oint_{\mathcal{L}(t-R/c_{\mathrm{L}})} \frac{1}{c_{\mathrm{L}}R(R - \mathbf{R}\cdot\mathbf{V}/c_{\mathrm{L}})} \left(\mathbf{b}\otimes(\mathbf{V}\times\boldsymbol{\xi}) - 3\frac{\mathbf{R}\otimes(\mathbf{V}\times\boldsymbol{\xi})(\mathbf{b}\cdot\mathbf{R})}{R^2}\right)\mathrm{d}L' \Bigg\}.\end{aligned} \tag{18}$$

Here $\boldsymbol{\Xi}_{kl}$ is defined as $\epsilon_{krl}\boldsymbol{\xi}_r$. R is the magnitude of $\mathbf{R}$, which is the vector connecting the source point to the observer point, namely, $\mathbf{R} = \mathbf{x} - \mathbf{x}'$. Here, $\mathbf{x}'$ is a source position on the retarded dislocation loop and $\mathcal{L}(t - R/c)$ represents the collection of retarded points $\boldsymbol{x}'$ on the loop such that,

$$\mathcal{L}(t - R/c) = \{\mathbf{x}' \text{ such that } \|\mathbf{x} - \mathbf{x}'(t_{\mathrm{ret}})\| = c(t - t_{\mathrm{ret}})\} \tag{19}$$

is the retarded loop seen at the observer point $\mathbf{x}$. t_{ret} is retarded time corresponding to a specific elastic wave velocity c, which may be c_{T}, c_{L}, or $1/\kappa$. $1/\kappa$ represents the elastic wave speed between c_{T} and c_{L}. It can be seen that all integrands in Eq. (18) are evaluated at the retarded time t_{ret}. This technique of using retarded potentials simplifies the calculation of coupled spatial and temporal integration to a spatial integral over retarded dislocation positions. This retarded potential method is standard in electrodynamics (Jackson, 2012; Landau and Lifshitz, 1971). In electrodynamics, if one uses the retarded Green's function, the corresponding solution for the potentials are the retarded potentials. For a non-uniformly moving point charge, the retarded potentials become the Lienard-Wiechert potentials. The retarded functions are the consequence of the finite speed of the wave and respect the effect of retardation. This idea is applicable to any dynamical theory with retardation, including elastodynamics (Lazar, 2013b). The simplest example is the well-known Doppler effect in acoustics.

By virtue of $\int \delta\left(f(t)\right) g(t)\mathrm{d}t = \frac{g(t)}{|\mathrm{d}f/\mathrm{d}t|}\,|_{f(t)=0}$, terms like $1/(R - \mathbf{R}\cdot\mathbf{V}/c_{\mathrm{T}})$ in Eq. (18) are obtained from

$$\int \frac{\delta\left(t - t' - |\mathbf{r}-\mathbf{r}'|/c_{\mathrm{T}}\right)}{R}\mathrm{d}t = \frac{1}{|R - \mathbf{R}\cdot\mathbf{V}/c_{\mathrm{T}}|}\,|_{t=t_{\mathrm{T}}}\,. \tag{20}$$

According to Eq. (18) and Eq. (3), the elastodynamic stress field induced by a non-uniformly moving dislocation loop is obtained as

$$\sigma(\mathbf{x},t) = \frac{\mu}{4\pi}\left(\mathbf{s}(\mathbf{x},t) + \mathbf{s}^{\mathrm{T}}(\mathbf{x},t)\right), \tag{21}$$

where the auxiliary tensor $\mathbf{s}(\mathbf{r},t)$ is given by,

$$\begin{aligned}
\mathbf{s}(\mathbf{x},t) = \oint_{\mathcal{L}(t-R/c_T)} &\frac{1}{R^2\left(R-\mathbf{R}\cdot\mathbf{V}/c_T\right)}\left(-2\mathbf{R}\otimes(\mathbf{b}\times\boldsymbol{\xi}) + \frac{-\nu}{1-2\nu}\mathbf{b}\cdot(\mathbf{R}\times\boldsymbol{\xi})\mathbf{I} - 3\left(\mathbf{b} - 4\frac{\mathbf{R}\cdot\mathbf{b}}{R^2}\mathbf{R}\right)\otimes(\mathbf{R}\times\boldsymbol{\xi})\right)\mathrm{d}L' \\
&-\partial_t\oint_{\mathcal{L}(t-R/c_T)}\frac{1}{c_T R\left(R-\mathbf{R}\cdot\mathbf{V}/c_T\right)}\left(\frac{\nu}{1-2\nu}\mathbf{b}\cdot(\mathbf{R}\times\boldsymbol{\xi})\mathbf{I} + \left(\mathbf{b} - \frac{2\mathbf{R}\cdot\mathbf{b}}{R^2}\mathbf{R}\right)\otimes(\mathbf{R}\times\boldsymbol{\xi})\right)\mathrm{d}L' \\
+\oint_{\mathcal{L}(t-R/c_L)} &\frac{1-2\nu}{(1-\nu)R^2\left(R-\mathbf{R}\cdot\mathbf{V}/c_L\right)}\left(\frac{1-3\nu}{1-2\nu}\mathbf{R}\otimes(\mathbf{b}\times\boldsymbol{\xi}) + \frac{\nu^2}{(1-2\nu)^2}\mathbf{b}\cdot(\mathbf{R}\times\boldsymbol{\xi})\mathbf{I} + \left(\mathbf{b} - \frac{6\mathbf{R}\cdot\mathbf{b}}{R^2}\mathbf{R}\right)\otimes(\mathbf{R}\times\boldsymbol{\xi})\right)\mathrm{d}L' \\
-\partial_t\oint_{\mathcal{L}(t-R/c_L)} &\frac{1-2\nu}{(1-\nu)c_L R\left(R-\mathbf{R}\cdot\mathbf{V}/c_L\right)}\left(\frac{\nu}{1-2\nu}\mathbf{R}\otimes(\mathbf{b}\times\boldsymbol{\xi}) - \frac{\nu^2}{(1-2\nu)^2}\mathbf{b}\cdot(\mathbf{R}\times\boldsymbol{\xi})\mathbf{I} + \left(\frac{\mathbf{R}\cdot\mathbf{b}}{R^2}\mathbf{R}\right)\otimes(\mathbf{R}\times\boldsymbol{\xi})\right)\mathrm{d}L' \\
&+\int_{1/c_L}^{1/c_T}\oint_{\mathcal{L}(t-R\kappa)}\frac{6c_T^2\kappa}{R^2\left(R-\mathbf{R}\cdot\mathbf{V}\kappa\right)}\left(\mathbf{R}\otimes(\mathbf{b}\times\boldsymbol{\xi}) + \left(\mathbf{b} - \frac{5\mathbf{R}\cdot\mathbf{b}}{R^2}\mathbf{R}\right)\otimes(\mathbf{R}\times\boldsymbol{\xi})\right)\mathrm{d}L'\mathrm{d}\kappa \\
&+\partial_t\oint_{\mathcal{L}(t-R/c_T)}\frac{1}{c_T^2\left(R-\mathbf{R}\cdot\mathbf{V}/c_T\right)}\left(\frac{\nu}{1-2\nu}\left(\mathbf{b} - \frac{\mathbf{R}\cdot\mathbf{b}}{R^2}\mathbf{R}\right)\cdot(\mathbf{V}\times\boldsymbol{\xi})\mathbf{I} + \left(\mathbf{b} - \frac{\mathbf{R}\cdot\mathbf{b}}{R^2}\mathbf{R}\right)\otimes(\mathbf{V}\times\boldsymbol{\xi})\right)\mathrm{d}L' \\
&+\partial_t\oint_{\mathcal{L}(t-R/c_L)}\frac{1}{c_L^2\left(R-\mathbf{R}\cdot\mathbf{V}/c_L\right)}\left(\frac{\nu}{1-2\nu}\left(\frac{\mathbf{R}\cdot\mathbf{b}}{R^2}\mathbf{R}\right)\cdot(\mathbf{V}\times\boldsymbol{\xi})\mathbf{I} + \left(\frac{\mathbf{R}\cdot\mathbf{b}}{R^2}\mathbf{R}\right)\otimes(\mathbf{V}\times\boldsymbol{\xi})\right)\mathrm{d}L' \\
&-\int_{1/c_L}^{1/c_T}\oint_{\mathcal{L}(t-R\kappa)}\frac{1}{R\left(R-\mathbf{R}\cdot\mathbf{V}\kappa\right)}\left(\frac{\nu}{1-2\nu}\left(\mathbf{b} - \frac{3\mathbf{R}\cdot\mathbf{b}}{R^2}\mathbf{R}\right)\cdot(\mathbf{V}\times\boldsymbol{\xi})\mathbf{I} + \left(\mathbf{b} - \frac{3\mathbf{R}\cdot\mathbf{b}}{R^2}\mathbf{R}\right)\otimes(\mathbf{V}\times\boldsymbol{\xi})\right)\mathrm{d}L'\mathrm{d}\kappa \\
&+\oint_{\mathcal{L}(t-R/c_T)}\frac{1}{c_T R\left(R-\mathbf{R}\cdot\mathbf{V}/c_T\right)}\left(\frac{\nu}{1-2\nu}\left(\mathbf{b} - \frac{3\mathbf{R}\cdot\mathbf{b}}{R^2}\mathbf{R}\right)\cdot(\mathbf{V}\times\boldsymbol{\xi})\mathbf{I} + \left(\mathbf{b} - \frac{3\mathbf{R}\cdot\mathbf{b}}{R^2}\mathbf{R}\right)\otimes(\mathbf{V}\times\boldsymbol{\xi})\right)\mathrm{d}L' \\
&-\oint_{\mathcal{L}(t-R/c_L)}\frac{1}{c_L R\left(R-\mathbf{R}\cdot\mathbf{V}/c_L\right)}\left(\frac{\nu}{1-2\nu}\left(\mathbf{b} - \frac{3\mathbf{R}\cdot\mathbf{b}}{R^2}\mathbf{R}\right)\cdot(\mathbf{V}\times\boldsymbol{\xi})\mathbf{I} + \left(\mathbf{b} - \frac{3\mathbf{R}\cdot\mathbf{b}}{R^2}\mathbf{R}\right)\otimes(\mathbf{V}\times\boldsymbol{\xi})\right)\mathrm{d}L'
\end{aligned} \tag{22}$$

and $\mathbf{s}^{\mathrm{T}}(\mathbf{x},t)$ is its transpose.

It is useful to verify the static limit of the above expression. To do so, we drop all the terms containing the velocity ($|\mathbf{V}|/c \to \mathbf{0}$), and let time go infinity, the retarded positions coincide with the current position $\mathcal{L}$. Thus, we obtain

$$\begin{aligned}
\sigma_{ij}(\mathbf{x}) = \frac{-\mu b_l}{4\pi(1-\nu)}\oint_{\mathcal{L}}\Bigg\{&\frac{1-2\nu}{2R^3}\left(\delta_{il}R_k\epsilon_{jks} + \delta_{jl}R_k\epsilon_{iks} - R_i\epsilon_{jls} - R_j\epsilon_{ils}\right) \\
&+\frac{3R_nR_l\left(R_i\epsilon_{jns} + R_j\epsilon_{ins}\right)}{2R^5} + \frac{2\nu\delta_{ij}R_n\epsilon_{lns}}{R^3}\Bigg\}\xi_s\mathrm{d}L'.
\end{aligned} \tag{23}$$

Upon substitution of position vector derivatives into Eq. (23), one obtains

$$\sigma_{ij}(\mathbf{x}) = \frac{\mu b_l}{4\pi}\oint_{\mathcal{L}}\left\{\frac{1}{2}\left(\epsilon_{jnl}\xi_i + \epsilon_{inl}\xi_j\right)R_{,npp} + \frac{1}{1-\nu}\epsilon_{snl}\xi_s\left(R_{,ijn} - \delta_{ij}R_{,npp}\right)\right\}\mathrm{d}L'. \tag{24}$$

This is the same as the widely-used formula of the stress field of a stationary dislocation derived by de Wit' (1960) [2].

3. Numerical Implementation in 3D-DDE

Due to the complexity of the elastodynamic field equations (such as Eq. (22)), the three-dimensional numerical implementation has never been carried out. For a 2D dislocation system, each dislocation line is simplified as a point such that a dislocation is considered similar to a charged particle. The proposed method is based on the elastodynamics induced by point sources, which is relatively well-developed. However, in the 3D-DDE methodology, a dislocation segment is the basic element describing a dislocation network. To the best of our knowledge, there are no reports detailing how to effectively and accurately treat moving line sources in elastodynamics. In the following, a numerical implementation procedure will be for the first time presented. It will be useful not only for dislocation systems, but also will shed light on treating other types of line sources in elastodynamics.

The 3D-DDE employed here is one part of the MoDELib (Mechanics Of Defect Evolution Library) computer code (Po and Ghoniem, 2015), which is described in detail in our previous papers (Cui et al., 2018; Po and Ghoniem, 2014a; Po et al., 2014b). In this 3D-DDE approach, curved dislocation lines are discretized into a succession of parametrized segments. Configurational Peach-Koehler forces are computed, and a system of equations for the motion of nodes connecting these segments is solved in a way similar to the traditional finite element method (FEM), as described in detail in (Po et al., 2014c). In the following, we will present an extension of the parametric method, previously developed for quasi-static dislocation ensembles, to the elastodynamic field emitted by moving dislocations of arbitrary shape. Note that the current method mainly focuses on subsonic motion of dislocations. The extension of the method to include dislocations moving at transonic or supersonic speeds is left for future work. In addition, the following results do not consider finite boundary effects. The boundary conditions and image forces can be included by coupling with an FEM solution of an elasticity problem using the superposition principle, following the method described in detail in our previous work (Po et al., 2014c).

3.1. Dislocation Motion History

Fundamental computational difficulties arise from the fact that the elastodynamic field is strongly history dependent, as shown in Eq. (22). This means that the entire history of dislocation motion must be recorded. In 3D-DDE, a dislocation network is composed of dislocation segments. As schematically shown in Fig. 1, one dislocation loop is discretized into several segments. To ensure a high level of spatial accuracy, each segment is further represented by a number of quadrature points, with a parameter u between 0 and 1 to specify the position along the segment. Generally, the spacing between quadrature points is on the order of the Burger's vector magnitude. More details about the quadrature point implementation in 3D-DDE are given in (Ghoniem et al., 2000; Po et al., 2014c). The dislocation position is updated according to the movement of many dislocation nodes at the beginning and end points of segments. Therefore, one natural choice is to record the motion history of dislocation nodes only, and enslave all points in-between the nodes by virtue of the parametrized geometry. In this fashion, the dynamics of the entire dislocation loop can be recovered from the motion of nodes at the beginning and end of each segment.

To keep the amount of data storage at a minimum, we introduce two key concepts. (i) Master-slave: in addition to recording the Burger's vector and slip plane normal information for a dislocation loop, we chose to only record the motion history of dislocation nodes, and utilize geometric parametrization to obtain the positions of all intervening points between nodes. (ii) Causality: to avoid the continuous increase of the motion history information, we consider a specific part of the temporal history of a dislocation loop, where the elastic field signals sent from far away distances are not tracked. To ensure causality, the following simple condition is carried out. At time t, if $c_{\mathrm{T}}(t-t')$ is larger than the maximum linear distance between dislocation loop and all possible observer points, we delete all motion history information before time t'.

---

[2] In this derivation, the relation $\epsilon_{ijk}\epsilon_{mnk} = \delta_{im}\delta_{jn} - \delta_{in}\delta_{jm}$ is frequently used. In addition, we note that $\oint_{\mathcal{L}} b_l\xi_s(\epsilon_{jnl}R_{,ins} + \epsilon_{inl}R_{,jns})\mathrm{d}L = 0$ according to Stoke's theorem. This implies that Eq. (23) is equivalent to Eq. (24) only for closed dislocation loops, whereas for an open dislocation line, the difference induced by the $\int_{\mathcal{L}} b_l\xi_s(\epsilon_{jnl}R_{,ins} + \epsilon_{inl}R_{,jns})\mathrm{d}L$ term must be considered.

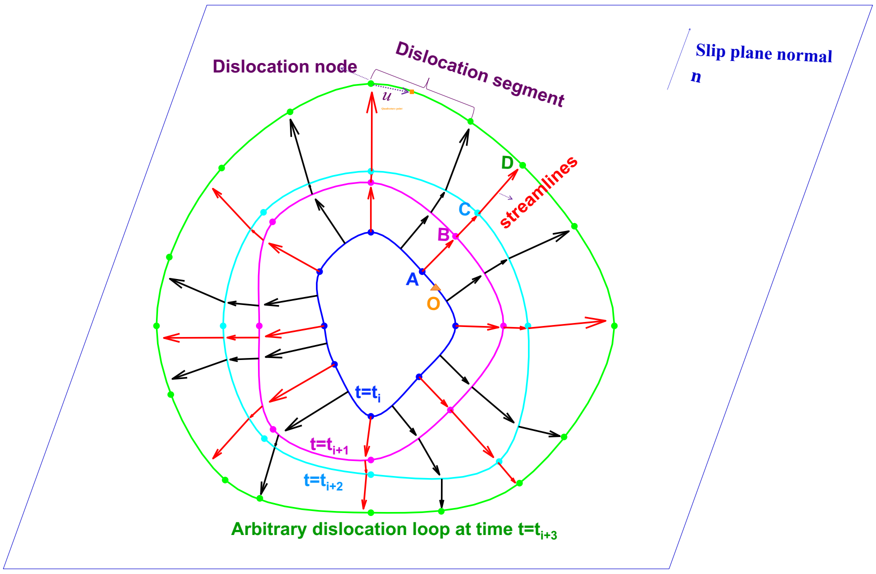

Figure 1: A dislocation loop at four times t, which are indicated by different colors. The loop is discretized in segments, which are further discretized into quadrature points. u is a parameter between 0 and 1 to specify the position along a dislocation segment. The solid arrows are called streamlines, which describe the elementary motion vector of an infinitely small part of a dislocation segment along the dislocation loop. The arrow head size is proportional to the velocity magnitude.

In the following, we will present a method for obtaining all required information, as long as the dislocation node position and connectivity information are recorded. The quantities of interest include the position, the local tangent direction, and the instantaneous velocity of an elementary dislocation segment. First, given the dislocation node position and connectivity information, the corresponding dislocation loop can be regenerated at each time according to a specific parametric form of splines (see section II in (Ghoniem and Sun, 1999) for more details). As an example, in Fig. 1, cubic Catmull-Rom splines are generated to connect discrete dislocation nodes. Meanwhile, the corresponding local tangent or normal direction of elementary dislocation segments are obtained. Secondly, one needs to accurately calculate the velocity of a line source, which different from a point source that has a well-defined velocity. The complexity of the line source resides in the possibility of length change as it moves. Therefore, for an arbitrarily infinite small line, its motion direction should be perpendicular to its local tangent direction, which we will assume for all points on the dislocation. If one only considers the glide motion of a dislocation, its driving force is the Peach-Koehler (PK) force $f_{\mathrm{PK}} = \sigma \cdot \mathbf{b} \times \boldsymbol{\xi}$. For a Volterra dislocation, the force is given by the PK expression in dynamics, in the same way as in statics (Stroh, 1962). This means that the driving force of dislocation motion, as well as the velocity direction are both perpendicular to the dislocation segment direction. However, the velocity of a dislocation node is not always perpendicular to the local tangent direction of a dislocation segment, because it actually reflects the contribution coming from both the segment velocity and the elongation or contraction of the segment itself. One example is shown in Fig. 2. For a straight dislocation, there is no difference between nodal velocity and segment velocity. However, we need to accurately calculate the segment velocity, which is suitable for the general case.

To circumvent this difficulty, we propose the streamline method. After knowing the dislocation loop information, we calculate the streamlines between each time increment. For example, starting from node A on a dislocation loop at time t_i in Fig. 1, according to the local tangent direction, it is easy to calculate its intersection point with the dislocation loop at time t_{i+1} (see point B in Fig. 1), where i represents the time step index. Since the time interval is very small, linear interpolation is used, so the corresponding velocity from time t_i to t_{i+1} is $|\mathrm{AB}|/(t_{i+1} - t_i)$. Similarly, one can calculate the intersection points C and D and their corresponding velocities. The line ABCD is called the streamline, which describes the motion history of an infinitely-small dislocation segment around node A. The number of streamlines depends on the required spatial resolution, and can be changed with the expansion or contraction of the dislocation loop. In Fig. 1, the red streamlines are generated from time t_i to t_{i+2}, while the black streamlines are generated since time t_{i+3} due to the significant expansion of the dislocation loop. For each dislocation loop,

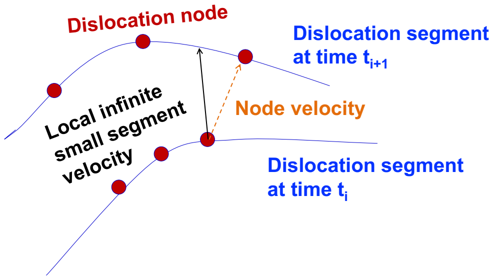

Figure 2: Schematic showing the difference between node velocity and segment velocity

their streamlines can be labeled by $l(p)$, here p is a number from 0 to 1. Assuming that t_i is the initial time for this dislocation loop, we chose a point O on the initial dislocation loop as shown in Fig. 1. Then, the number p of streamline ABCD is calculated by dividing the arc length of OA by the perimeter of the whole loop. The arc length orientation (clockwise or counterclockwise) is determined according to the slip plane normal direction and right hand rule. This makes it easier to add new streamlines between original ones. Therefore, in addition to the advantage of accurately calculating the segment velocity, another advantage of using the streamline method is that re-meshing or topology treatment will be facilitated, since we can easily use more streamlines to get better spatial resolution. This is particularly important, because in 3D-DDE, the dislocation node may disappear or appear due to the length change of the segment, or the dislocation interaction. The robustness with respect to such topology treatment is highly required.

For the glide motion of a straight dislocation line, the streamline may be consistent with the trajectory of a dislocation node. However, as shown in Fig. 1, sometimes, the streamline may not be consistent with the trajectory of a dislocation node. This is similar to the possible difference between a streamline and a pathline in fluid mechanics. When the discrete dislocation segment is small enough, the trajectory of a dislocation node is a good approximation of the streamline. Therefore, for a 3D-DDE code using straight dislocation segments, one may use the trajectory of a dislocation node to approximate the dislocation streamline if more nodes are used, and the presented method in the following sections is also applicable. Special care is then needed to deal with topology changes.

3.2. *Determination of Retarded Times* & Positions

If one sees a star that is a few million light years away, that would be observing its *retarded position*, since it has moved to a different current position! We consider here a similar computational problem. One of the key issues is the determination of three retarded times, namely, t_T, t_L, and t_κ, corresponding to c_T, c_L, $1/\kappa$, and appearing in Eq. (22). This requires a numerical solution of Eq. (19). For subsonic dislocation motion, there is one and only one retarded time solution for each dislocation streamline, corresponding to a specific observer point, recipient time t and wave velocity c in Eq. (19). As shown in Fig. 3 (a), it is assumed that the retarded position of a dislocation streamline $l(p)$ is D, when the recipient time is t and the observer point is P. According to Eq. (19), $|\mathrm{PD}| = c(t - t_\mathrm{ret})$. Let us assume that there is another point C that also meets Eq. (19), such that $|\mathrm{PC}| = c(t - t_\mathrm{ret} - \Delta t_{DC})$, where Δt_{DC} is the time difference corresponding to point D and point C. It is easy to prove that this is impossible, since $|\mathrm{PD}| + |\mathrm{CD}| < |\mathrm{PC}|$ as long as the dislocation velocity is subsonic ($V < c_\mathrm{T}$).

Even though many efforts have been carried out to determine the retarded time for a moving source (Carley, 2003; Casalino, 2003), t_ret cannot generally be calculated analytically nor easily (Lazar, 2013b). Here, we propose a root-finding algorithm to evaluate t_ret according to the trajectory information of dislocation nodes. Before estimating t_ret, a simple calculation is carried out to check whether this dislocation streamline may influence the observer P. Taking the dislocation streamline $l(p)$ in Fig. 3(a) as an example, without loss of generality, one can say that the corresponding infinitely-small dislocation segment moves from point A to point B, corresponding to time t_A and t_B, respectively. If $|\mathrm{PA}| > c(t - t_A)$ or $|\mathrm{PB}| < c(t - t_B)$, the elastodynamic perturbations induced by dislocation streamline $l(p)$ cannot reach the observer P at time t. Therefore, further calculation is only carried out if the following conditions are met,

$$|\mathrm{PA}| \leq c(t - t_A) \quad \text{and} \quad |\mathrm{PB}| \geq c(t - t_B) \tag{25}$$

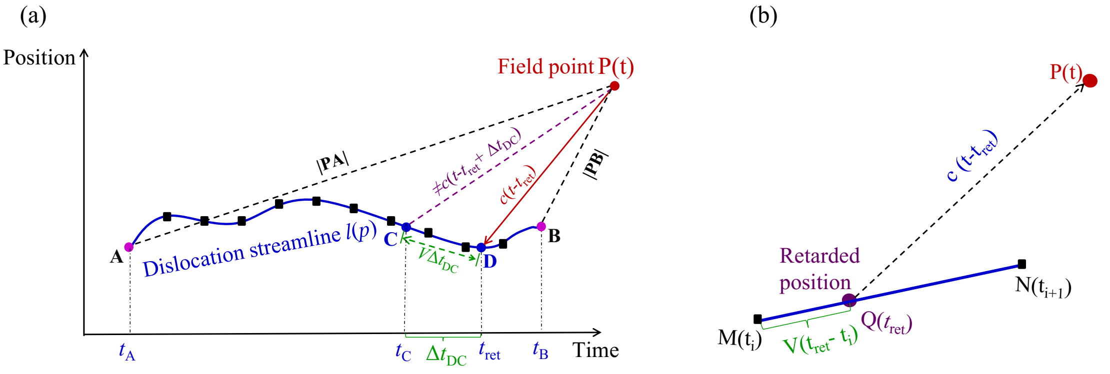

Figure 3: (a) Schematic showing the dislocation streamline l(p) and observer point P; (b) Determination of the retarded time for quadrature point Q after the closest time interval is found.

If Eq. (25) is met, an iterative bisection method is used to find the closest time interval. Namely, one repeatedly bisects the time interval and then selects a subinterval in which Eq. (25) is met for the ending points of that subinterval, until the interval corresponds to two consecutive time steps, such as $[t_{\mathrm{i}}, t_{\mathrm{i+1}}]$, is found. Considering that the retarded times of neighboring dislocation nodes are close, the calculated retarded time information will be used as a starting point for the calculation of its neighboring dislocation nodes, for more rapid convergence. Afterwards, between continuous time incremental steps $[t_{\mathrm{i}}, t_{\mathrm{i+1}}]$, the velocity $\mathbf{V}$ is assumed to be constant because of the very small time interval. Then, an analytical solution is used to determine its retarded time t_{ret}, as shown in Fig. 3(b),

$$
\begin{aligned}
&|\mathrm{Q}-\mathrm{P}| = |\mathrm{M}+\mathbf{V}(t_{\text{ret}}-t_i)-\mathrm{P}| = c(t-t_{\text{ret}}) \\
&t_{\text{ret}} = \frac{c^2 t-(\mathbf{V}\cdot\mathbf{V})t_i+(\mathrm{M}-\mathrm{P})\cdot\mathbf{V} \pm \sqrt{[c^2(t-t_i)+(\mathrm{M}-\mathrm{P})\cdot\mathbf{V}]^2-(c^2-\mathbf{V}\cdot\mathbf{V})[c^2(t-t_i)^2-(\mathrm{M}-\mathrm{P})\cdot(\mathrm{M}-\mathrm{P})]}}{c^2-\mathbf{V}\cdot\mathbf{V}},
\end{aligned}
\tag{26}
$$

where Q, P, M represent their position vectors. Along each dislocation streamline, one may find zero or one retarded position. Therefore, for each neighboring dislocation streamline pair, one may obtain two retarded positions (see Fig. 4(a)), one retarded position (see Fig. 4(b)), or no retarded position (see Fig. 4(c-d)). In the following, each of these cases will be discussed in detail. The reason why we care about the retarded position number corresponding to neighboring streamline pairs is because line integrations in Eq. 22 are along the segment connecting neighboring retarded positions. This will be further discussed in the next section.

- Case 1: If two retarded positions are found, as shown in Fig. 4(a), all nodes between A and B will influence the observer point.

- Case 2: If the retarded position is only found for one dislocation streamline, such as shown in Fig. 4(b), this means that only part of the dislocation nodes between A and B affects the observer point P. Assuming that a dislocation segment AB appears since time t_0, its position at time t_0 is expressed as $\mathrm{A_0B_0}$ in Fig. 4(b). Obviously, $\mathrm{A_0B_0}$ corresponds to the earliest and farthest radiated elastic perturbation. Therefore, the critical retarded points C_r along dislocation spline that can reach receiver P must belong to $\mathrm{A_0B_0}$. The position of C_r can be analytically calculated based on the relation $|\mathrm{PC}_r| = c(t-t_0)$, where $|\mathrm{PC}_r|$ represents the distance between the receiver P and C_r.

- Case 3: if the retarded position is not found for either dislocation streamline, there is still a possibility that elastodynamic perturbations induced by this dislocation spline AB reach the observer P at time t. As shown in Fig. 4(c), point C_r and D_r happen to reach observer point P at time t, which means $|\mathrm{PC}_r| = c(t-t_0)$ and $|\mathrm{PD}_r| = c(t-t_0)$. Therefore, one needs to calculate the minimum distance between the initial dislocation spline

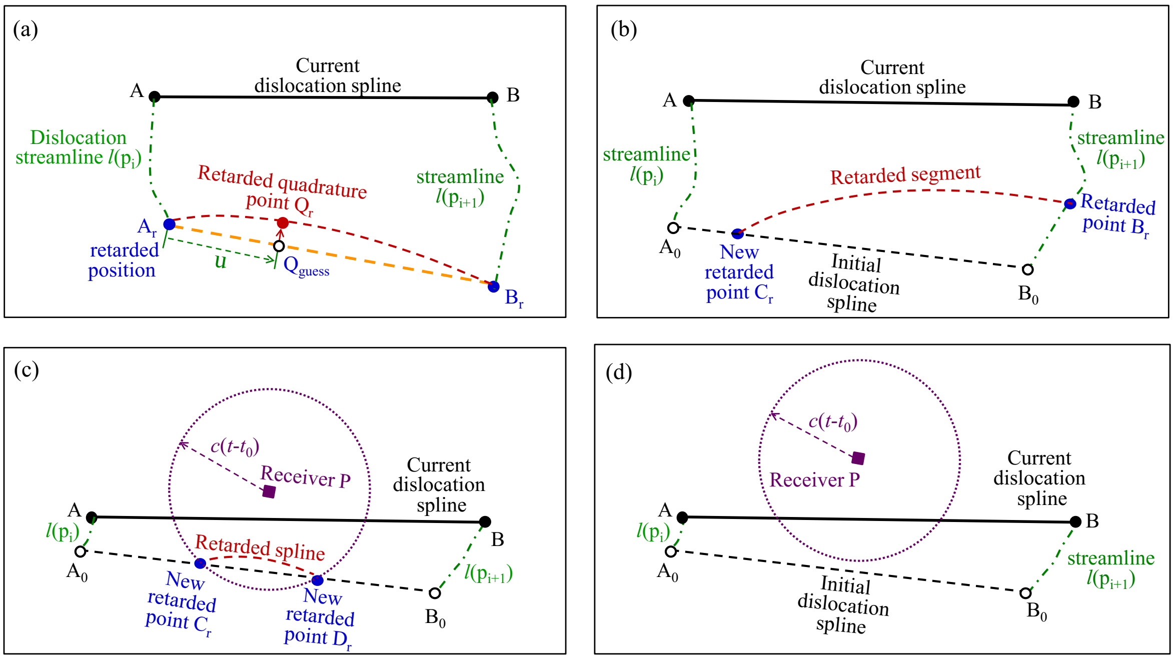

Figure 4: Schematic showing the method of generating retarded quadrature points. (a) when the retarded position is only found for one dislocation node, a new retarded position needs to be determined. (b) Retarded segments are generated according to the end retarded positions A_r and B_r.

A_0B_0 and observer point P, if this distance is smaller than $c(t-t_0)$, two retarded points can be found along A_0B_0, as shown in Fig. 4(c). If the distance is equal to $c(t-t_0)$, only one retarded point reaches observer point P. It is reasonable to ignore this case, because a single point source does not influence the calculation of a line integral. On the other hand, if this distance is larger than $c(t-t_0)$, no retarded points can be found, as shown in Fig. 4(d). This means that elastodynamic perturbations induced by this dislocation segment cannot reach the observer P at recipient time t. Thus, no further calculations are required. A parallel architecture can be used to accelerate the calculation process of retarded times. Therefore, for each neighboring dislocation streamline pair, further calculations are required only when two retarded positions are found.

3.3. *Fast Sum Implementation of Line Integrals*

The line integral over retarded dislocation loops in Eq. (22) can be converted into a fast numerical sum (Ghoniem and Sun, 1999) over the retarded quadrature points. If two retarded positions are found for neighboring dislocation streamline pair, such as A_r and B_r in Fig. 4(a), C_r and B_r in Fig. 4(b), and C_r and D_r in Fig. 4(c). A virtual retarded dislocation spline is generated between these two retarded positions. Then, quadrature points are generated along these retarded dislocation segments with a spacing on the order of b.

Note that each quadrature point uses the dislocation spline information at its retarded time ($t_{\text{ret}}(u)$), including the position ($Q(u)$), tangent direction ($\xi(u)$), motion velocity ($\mathbf{V}(u)$), and weight factor ($w(u)$). Here, u is a parameter between 0 and 1 to specify the position along the dislocation segment, as shown in Fig. 4(a). Special care should be made if one simply uses an interpolation method to obtain $t_{\text{ret}}(u)$, $Q(u)$, and $\mathbf{V}(u)$ according to the end point information, since this cannot meet the retarded condition described by Eq. (19). Therefore, we propose a quick and effective approximation method to calculate the retarded position for each quadrature point. The basic idea is that if two neighboring retarded positions are very close, their retarded time should also be very close. Therefore, one can firstly use the interpolation method corresponding to the spline type to obtain an estimated retarded position, for example point Q_{guess} in Fig. 4(a). Its corresponding time t_{guess}, and velocity V_{guess} is easy to be obtained. Since t_{guess} should be close to the actual retarded time $t_{\text{ret}}(u)$, it is reasonable to assume that from t_{guess} to $t_{\text{ret}}(u)$, the velocity V_{guess} keeps constant. Then, the analytical solution presented in Eq. (26) can be used to calculate the $t_{\text{ret}}(u)$. After the retarded time is determined, all other information can be easily obtained. Then, the line integral becomes a fast numerical sum over quadrature points ($1 \leqslant \alpha \leqslant Q_{max}$) associated with loop segments ($1 \leqslant \beta \leqslant N_s$) and number of ensemble loops ($1 \leqslant \gamma \leqslant N_{\text{loop}}$) ,

$$\oint_{L(t')} f(\mathbf{R}, \mathbf{b}, \mathbf{V})\mathrm{d}L_k|_{t'=t_{\text{ret}}} = \sum_{\gamma=1}^{N_{\text{loop}}} \sum_{\beta=1}^{N_s} \sum_{\alpha=1}^{Q_{max}} f(\mathbf{R}, \mathbf{b}, \mathbf{V}) w_\alpha \hat{x}_{k,u}|_{t'=t_{\text{ret}}} \tag{27}$$

The form of the parametric description of dislocation segments is discussed in detail in (Ghoniem and Sun, 1999). Here, the cubic spline parametric representation is used to describe the dislocation segment. The integration over κ in the fifth and eighth line of Eq.(22) is calculated by performing a Riemann sum with respect to a tagged partition of the integration range $[1/c_{\mathrm{T}}, 1/c_{\mathrm{L}}]$,

$$\int_{1/c_{\mathrm{L}}}^{1/c_{\mathrm{T}}} f(\mathbf{R}, \mathbf{b}, \mathbf{V})\mathrm{d}\kappa|_{t'=t_\kappa} = \sum_{\eta=1}^{N_\kappa} \Delta_\eta \left(f(\mathbf{R}, \mathbf{b}, \mathbf{V})|_{t'=t_\eta} \right) \tag{28}$$

where the interval $[1/c_{\mathrm{T}}, 1/c_{\mathrm{L}}]$ is partitioned into N_κ sub-intervals $[\kappa_{\eta-1}, \kappa_\eta]$ indexed by η. Δ_η is the width of the subinterval η, $\Delta_\eta = \kappa_\eta - \kappa_{\eta-1}$. Here, $N_\kappa = 8$ is used.

Alternatively, Simpson's rule is also a good choice due to its higher precision,

$$\int_{1/c_{\mathrm{L}}}^{1/c_{\mathrm{T}}} f(\mathbf{R}, \mathbf{b}, \mathbf{V})\mathrm{d}\kappa|_{t'=t_\kappa} = \sum_{\eta=1}^{N_\kappa} \frac{\Delta_\eta}{6} \left(f(\mathbf{R}, \mathbf{b}, \mathbf{V})|_{t'=t_{\eta-1}} + 4 f(\mathbf{R}, \mathbf{b}, \mathbf{V})|_{t'=t_{\eta-0.5}} + f(\mathbf{R}, \mathbf{b}, \mathbf{V})|_{t'=t_\eta} \right) \tag{29}$$

where $t_{\eta-1}$, $t_{\eta-0.5}$, and t_η represent the retarded time corresponding to wave speed $1/\kappa_{\eta-1}$, $2/(\kappa_{\eta-1} + \kappa_\eta)$, and $1/\kappa_\eta$, respectively.

3.4. Computation of Time Derivatives

Special care should be taken when calculating the time derivative terms in Eq. (22) (such as those on the second and fourth lines). Firstly, the line integral range is a function of time, which means that a moving boundary is involved. Secondly, the integrand is possible to be singular at the integration range boundary. The transport theorem of line integrals (Scovazzi and Hughes, 2007) is usually used to deal with the moving boundary integration problem. The time derivative can be calculated as follows:

$$\partial_t \oint_{L(t')} f(\mathbf{R}, \mathbf{b}, \mathbf{V})\mathrm{d}\mathbf{L}|_{t'=t_{\text{ret}}} = \oint_{L(t')} \frac{\partial f(\mathbf{R}, \mathbf{b}, \mathbf{V})}{\partial t}\mathrm{d}\mathbf{L}|_{t'=t_{\text{ret}}} + \oint_{L(t')} f(\mathbf{R}, \mathbf{b}, \mathbf{V})(\nabla_x V)\mathrm{d}\mathbf{L}|_{t'=t_{\text{ret}}}. \tag{30}$$

Note that Eq. (30) is more suitable for a total time derivative. However, since $f(\mathbf{R}, \mathbf{b}, \mathbf{V})$ has no explicit time dependence,[3] the total or partial derivative for that function should be the same. The difficulty of using Eq. (30) lies in two aspects. (1) The interchange of the order of differentiation and the integration can only be done when the differentiation of the integrand does not introduce non-integrable singularities (Markenscoff and Clifton, 1981). For the case considered here, $\partial f/\partial t$ in the first term on the right hand side may have a stronger singularity. (2) when calculating the second term on the right hand-side, one needs to consider not only the motion of the dislocation line, but also the change of the influenced region, because sometimes only part of the dislocation line influences the field point.

On the other hand, it is more straightforward to calculate the time derivative term by evaluating the integral twice at two intervals t' and $t' - \mathrm{d}t'$ and taking the difference. By analyzing the time derivative terms in Eq. (22), we design

---

[3] One can express $f(\mathbf{R}(t), \mathbf{b}, \mathbf{V}(t))$, but not $f(\mathbf{R}(t), \mathbf{b}, \mathbf{V}(t), t)$

a very simple, yet effective benchmark case to validate the time derivative calculation. Assuming that we consider an infinitely-long straight dislocation line along x_3 at rest, i.e its velocity is zero. For a field point at $(x_1, x_2, 0)$,

$$\partial_t \oint_{\mathcal{L}(t-R/c_{\mathrm{T}})} \frac{1}{R\left(R - \mathbf{R}\cdot\mathbf{V}/c_{\mathrm{T}}\right)} \mathrm{d}L' = \partial_t \int_{-\sqrt{c_{\mathrm{T}}^2 t^2 - l^2}}^{\sqrt{c_{\mathrm{T}}^2 t^2 - l^2}} \frac{1}{R^2} \mathrm{d}x_3 = \partial_t \left(\frac{2}{l} \arctan\left(\frac{\sqrt{c_{\mathrm{T}}^2 t^2 - l^2}}{l} \right) \right) = \frac{2}{t\sqrt{c_{\mathrm{T}}^2 t^2 - l^2}} \mathrm{H}(c_{\mathrm{T}} t - l), \tag{31}$$

where $l^2 = x_1^2 + x_2^2$. H(x) is Heaviside step function. Eq. (31) implies that there is a square root singularity at the wave front.

In the following, several numerical results will be presented and compared with the analytical solution of Eq. (31) to validate the time derivative term calculation and guide the accurate choice of the time interval $\mathrm{d}t'$. In the benchmark case, the integral $\int_{\mathcal{L}(t-R/c_{\mathrm{T}})} 1/R^2 dL'$ is first calculated twice at times t' and $t' - \mathrm{d}t'$ using the fast sum implementation presented in section 3.3. The calculation results are presented in Fig. 5 when the current time t is set to $200b/c_{\mathrm{T}}$. The field point has the same $x_2 = 0.2b$, while the x_1 varies as shown in the abscissa in Fig. 5. $\mathrm{d}l$ in Fig. 5 is the characteristic distance between quadrature points when one discretizes the retarded dislocation segments. It is very interesting that good results can only be observed when $\mathrm{d}l/c_{\mathrm{T}} < \mathrm{d}t' < \min(t/10, 100\ \mathrm{d}l/c_{\mathrm{T}})$. For example, in Fig. 5 (a), $\mathrm{d}l$ is fixed at 10^{-3}b, good results are obtained when $10^{-3}b/c_{\mathrm{T}} < \mathrm{d}t' < 0.1b/c_{\mathrm{T}}$. In contrast, if $\mathrm{d}t'$ is taken at smaller values, spurious singularities at arbitrary positions are observed when $\mathrm{d}t' = 0.1(\mathrm{d}l/c_{\mathrm{T}})$ (see $\mathrm{d}t' = 10^{-4}b/c_{\mathrm{T}}$ in Fig. 5 (a) or $\mathrm{d}t' = 10^{-2}b/c_{\mathrm{T}}$ in Fig. 5 (b)), or bad results with no singularity are observed when $\mathrm{d}t' = 10^{-2}\mathrm{d}l/c_{\mathrm{T}}$ (see $\mathrm{d}t' = 10^{-3}b/c_{\mathrm{T}}$ in Fig. 5 (b)). If $\mathrm{d}t'$ is taken as a larger value, greater errors are observed near the wave front region. This is to say that the magnitude of $\mathrm{d}t'$ determines the width of the region where the singularity is observed near the wave front. The value of $\mathrm{d}t'$ needs to be compatible with the magnitude of $\mathrm{d}l$.

The strong correlation between $\mathrm{d}t'$ and $\mathrm{d}l$ can be understood as follows. Firstly, all terms in the Green's tensor contain delta functions $\delta\left(t - \frac{x}{c}\right)$, hence the temporal and spatial variables are strongly coupled in nature. In Eq. (31), such temporal and spatial coupling is manifest in the integration range, which is a function of both time and position. Therefore, it is reasonable that the time interval $\mathrm{d}t'$ is strongly correlated with the value of $\mathrm{d}l$. When $\mathrm{d}t'$ is taken as a much smaller value, the resolution of the integral using the fast sum method is not good enough due to the relatively large $\mathrm{d}l$. Thus, good results cannot be obtained. On the other hand, when $\mathrm{d}t'$ is larger, the near wave front region, whose distance to the wave front is smaller than $c\mathrm{d}t'$, cannot be accurately calculated because the integral will be zero at such region at $t - \mathrm{d}t'$, but not at t. Therefore, to obtain good results, one can use the same $\mathrm{d}t'$ everywhere, as long as $\mathrm{d}l/c_{\mathrm{T}} < \mathrm{d}t' < \min(t/10, 100\ \mathrm{d}l/c_{\mathrm{T}})$. From Fig. 5 (a-b), one can also chose to use a relatively large $\mathrm{d}t'$ (as along as $\mathrm{d}l/c_{\mathrm{T}} < \mathrm{d}t' < t/10$) far from the wave front region, but small $\mathrm{d}t$ (as long as $\mathrm{d}l/c_{\mathrm{T}} < \mathrm{d}t'$) near the wave front region, depending on the required resolution. On the other hand, if one wants to use small $\mathrm{d}t'$, $\mathrm{d}l$ can also be changed to be small, as shown in Fig. 5 (c). This obviously implies more computational cost.

3.5. *Singularity Treatment*

There are two kinds of stress field singularities induced by a non-uniformly moving dislocation. The singularity at the wave front is found to be dominated by the time derivative terms in Eq. (22), which can be understood from the simple benchmark case of Eq. (31). As discussed in section 3.4, the reasonable choose of $\mathrm{d}t'$ is important to correctly capture and regularize the singularity at the wave front. On the other hand, Eq. (22) clearly shows that when the field point is located at the retarded position, $R = 0$, there is a strong singularity due to the existence of $1/R^n$, where n is an integer. A similar singularity is also widely observed for stationary dislocations. Cai et al. (2006) proposed replacing R and its derivatives with $R_a = \sqrt{R^2 + a^2}$ and its derivative, where a is the dislocation core size to regularize the field solution. The underlying physical reason of such treatment is that the Burger's vector is expressed as a distributed function. On the other hand, Lazar (2013a, 2014) proposed the regularization function $A(R) = R + 2l^2/R(1 - e^{-R/l})$ based on gradient elasticity theory. Here, l is a characteristic length in gradient elasticity, which is a material parameter that can be determined based on atomistic calculation results. For example, $l = 0.61a_l$ for W, $l = 0.49a_l$ for Al (Po et al., 2014b, 2018), and a_l is the lattice parameter of cubic crystals.

The strong coupling between time and space in the elastodynamic stress field renders the problem much more complicated. For the 2D infinitely-long dislocation, Pellegrini (2012); Pellegrini and Lazar (2015) proposed an effective regularization method by convolution of the 2D Green's tensor with a nonsingular Dirac distribution function (see

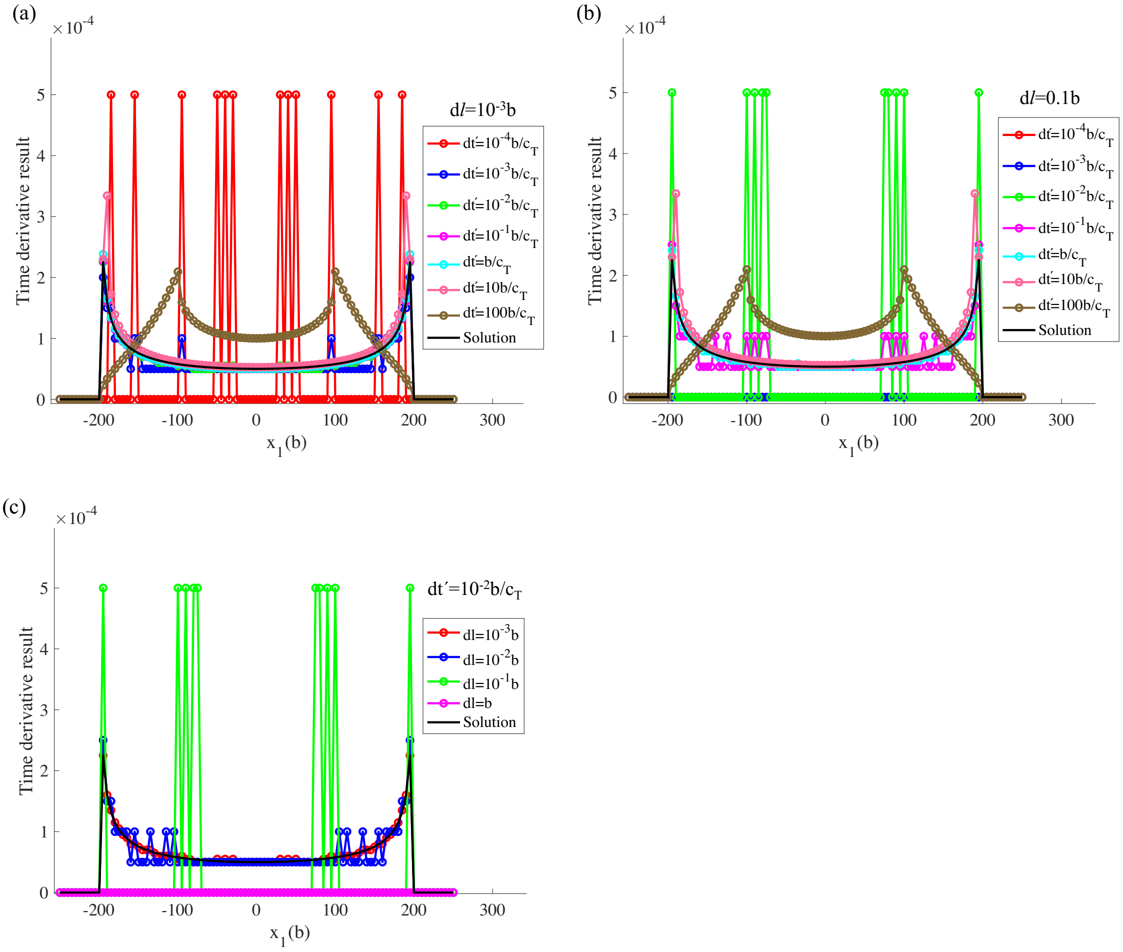

Figure 5: Numerical calculations compared to analytical results of Eq. (31) (a) for fixed spatial discretization distance between quadrature points $\mathrm{d}l = 10^{-3}b$, (b) for fixed $\mathrm{d}l = 0.1b$, (c) for fixed time interval $\mathrm{d}t' = 10^{-2}b/c_\mathrm{T}$. The field point is located at $(x_1, 0.2b, 0)$ and the dislocation line is located at $(0, 0, x_3)$.

Eq. (33) in (Pellegrini and Lazar, 2015)). This allows the equations to be amenable to a further extension to the supersonic regime. However, for the 3D-case, it is difficult to directly apply this technique. The reason is that in 3D, when calculating the stress field, one first makes a convolution of the Green's tensor with time, so the Dirac-delta function $\delta\left(t - t' - \frac{x(t')}{c}\right)$ is convoluted in time. Then, one only needs to calculate the results corresponding to one retarded time t_ret, which meets $t - t_\mathrm{ret} - \frac{x(t_\mathrm{ret})}{c} = 0$. If the singular Dirac-delta function is convoluted with a distribution, then, multiple retarded times need to be considered, rendering the problem computationally intractable with the present method. In contrast, in 2D, the assumption of the infinitely-long straight dislocation line simplifies the problem. The stress field is not calculated by integrating along the retarded segments, but is evaluated by integrating with respect to time (such as Eq. (44) in (Lazar and Pellegrini, 2016)). Thus, the introduction of a distribution function does not induce extra computational efforts. More discussion about the comparison between 3D and 2D elastodynamic Green's function and dislocation stress field will be discussed in a separate subsequent paper. In the current work, we simply replace the spatial derivatives with Cai et al.'s nonsingular counterparts as shown in Appendix B. More strict non-singular formulation of the stress field equation requires further dedicated future efforts.

Note that it is not easy to strictly deal with the dislocation core singularity based on the retarded potential method, since one needs to consider the retarded interactions within the core for any piece of dislocation interacting with itself, at least within continuum mechanics. Therefore, this problem cannot be addressed rigorously by starting from formulas valid for a Volterra dislocation, and afterwards carrying out a phenomenological regularization. One needs to start from a consistent expression for an extended (i.e., Somigliana) dislocation. As a consequence, the true rigorous retarded fields are more complicated. Thus for an extended (Somigliana, or regularized) dislocation, the retarded-time approach used in the current work is only an approximation.

4. Validation tests

In this section, several simple tests are presented to benchmark the 3D-DDE method. The straight dislocation line shown in Fig. 6 (a) is taken as an example, so as to compare with corresponding 2D solutions published in the literature.

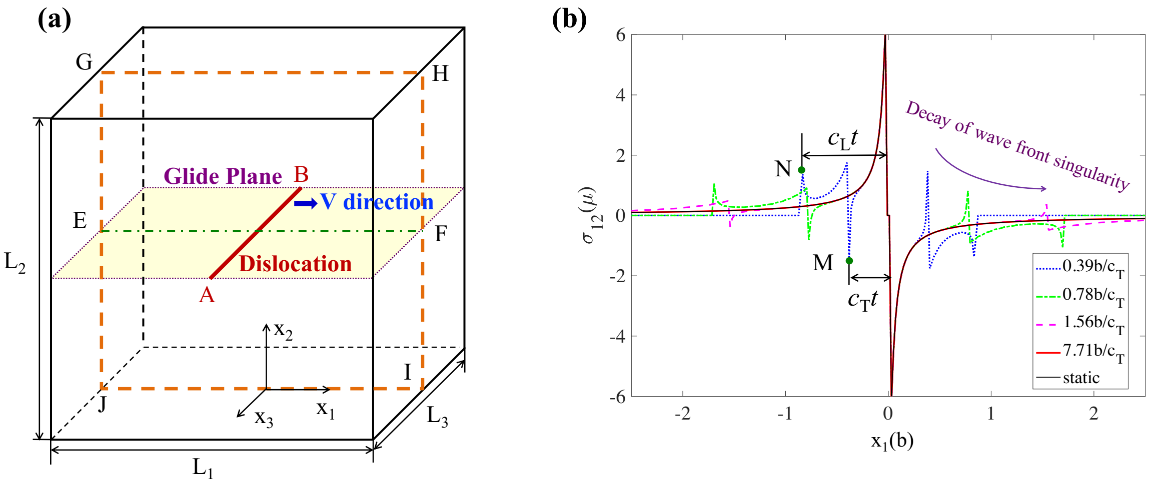

Figure 6: (a) Schematic showing the simulation case of a straight dislocation, (b) σ_{12} distribution along the line EF (x_2=0.01b, x_3=0) in (a) induced by a static straight edge dislocation at various times

4.1. Determination of the Retarded Dislocation Segment

Consider that a straight dislocation in Fig. 6 (a) has an initial zero velocity, then suddenly moves with high speed V from $t = 0$. The shapes of the retarded positions corresponding to points on the dislocation (we will denote this as the *retarded dislocation segment*) at two different speeds ($V = 0.3c_T$ and $V = 0.8c_T$) are shown in Fig. 7, for a observer point P [0.26 μm, 0, 0] at time t=0.1 ns and t=0.2 ns. From Fig. 7, the numerical solution (circle and triangular hollow points) is consistent with the analytical solution (red and green thick lines) given by Eq. (26). There are two features to note from Fig. 7. Firstly, even though the considered dislocation line is straight, the retarded dislocation segment that the observer point P experiences is not straight. Comparing Fig. 7(a) and (b), the higher the velocity of the straight dislocation, the more curved the retarded dislocation. Secondly, because the elastodynamic perturbations induced by the moving dislocation have not completely reached the observer point, only the curved part of the retarded dislocation in Fig.7 correspond to the history of moving with V, while the straight part with $x_1 = 0$ corresponds to the history of initial zero velocity. The curved part of the retarded dislocation is of finite length, which expands as time increases. Thus, to a stationary observer at P, the infinitely-long and straight dislocation is "experienced" as a curved dislocation, where higher apparent curvatures are associated with higher speeds!

4.2. The Injected Static Edge Dislocation

In the following, we will also discuss the case of a suddenly injected dislocation, where a hypothetical dislocation is assumed to suddenly appear at $t = 0$. If the injected dislocation suddenly moves at high-speed V from $t = 0$, its corresponding retarded dislocation only contains the curved part in Fig. 7. Since there is no history before $t = 0$, no straight retarded dislocations corresponding to zero velocity would exist.

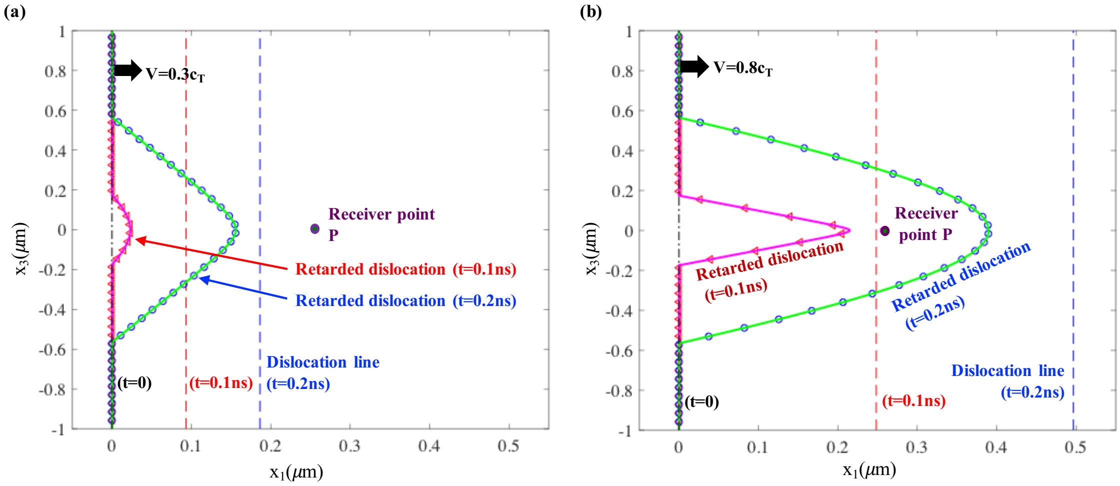

Figure 7: Examples showing the retarded dislocation for a moving straight dislocation with velocity V along the x_1-direction, (a) $V = 0.3c_T$ and (b) $V = 0.8c_T$. The circle and triangle hollow points designate retarded dislocation positions corresponding to $t = 0.1$ ns and $t = 0.2$ ns, respectively, while the red and green thick solid lines are the corresponding analytical solutions given by Eq. (26).

Table 1: Simulation parameters

Shear modulus μ	Poisson's ratio ν	Density ρ	Burger's vector magnitude b
26 GPa	0.3698	2700 kg/m^3	0.2851 nm

In order to verify the implementation of the elastic field in full-blown 3D DDE, the stress field induced by a static edge dislocation is first studied. The material parameters are listed in Table 1 for Al. The calculated dislocation stress component σ_{12} along the line EF in Fig. 6 (a) is shown at various times in Fig. 6 (b), where the steady-state result obtained by Eq. (23) is also given for comparison. Fig. 6 (b) illustrates that when the time t is $7.71b/c_T$, the dislocation stress field is almost the same as the static solution in the considered spatial range. However, from Fig. 6 (b), when t is shorter than $1.56b/c_T$, two singularities around the wave front are observed. This actually reflects the characteristic two-wave structure of the solution, where a precursor wave precedes the motion. Namely, one wave propagates at the longitudinal wave speed c_L, while the other propagates at the slower transverse wave speed c_T, and both of them radiate outward from the dislocation core. Taking t=0.39 b/c_T and the part of $x < 0$ as an example, the distances between the dislocation core and the two stress peaks correspond to $c_L t$ and $c_T t$, respectively, as indicated by points N and M in Fig.6 (b). These describe the elastodynamic perturbation range of the dislocation for the specific time. Outside the $c_L t$ region, the shear stress is zero for the injected edge dislocation. In addition, the comparison between the stress values at the wave front shows that the singularity gradually decreases with time. In Fig.6 (b), the curved arrow line shows the trend for the stress value at the transverse wave front.

Color plots of σ_{12} in x_1x_2 plane are further given in Fig. 8 (a-d). The characteristic two-wave structure at small t is manifested by two rings with radius $c_L t$ and $c_T t$. Fig. 8 (e-h) further presents the corresponding 2D nonsingular elastodynamics solutions, which are independently calculated by Eqs. (70a) and (70b) in (Lazar and Pellegrini, 2016) [4]. Note that the first term in Eqs. (70a) and (70b) in (Lazar and Pellegrini, 2016) is dropped when only considering the injection contribution. Here,"injection" means that the dislocation is assumed to suddenly nucleate without any previous history. On the other hand, the first term needs to be added when one considers that the dislocation starts from a steady state of constant initial velocity $\mathbf{V}_0$, such as initially static dislocation with zero velocity. Fig. 8 demonstrates very good agreement between the 3D-DDE and the 2D solutions of σ_{12} for all considered times. Moreover, Fig . D1 in Appendix D shows very good agreement between 3D and 2D calculations for different stress components at the

---

[4] The benchmark cases are designed to compare with the results of Gurrutxaga-Lerma et al. (2013). Since we observed some differences from their results, we carry out multiple independent dedicated 2D calculations to verify our current 3D-DDE results.

same time. In order to further clearly check the difference between 2D and 3D calculations, we investigated the stress field map of the 2D results minus the 3D results. Only small observable differences were found around the wave front and the dislocation core region, which are associated with different regularization methods.

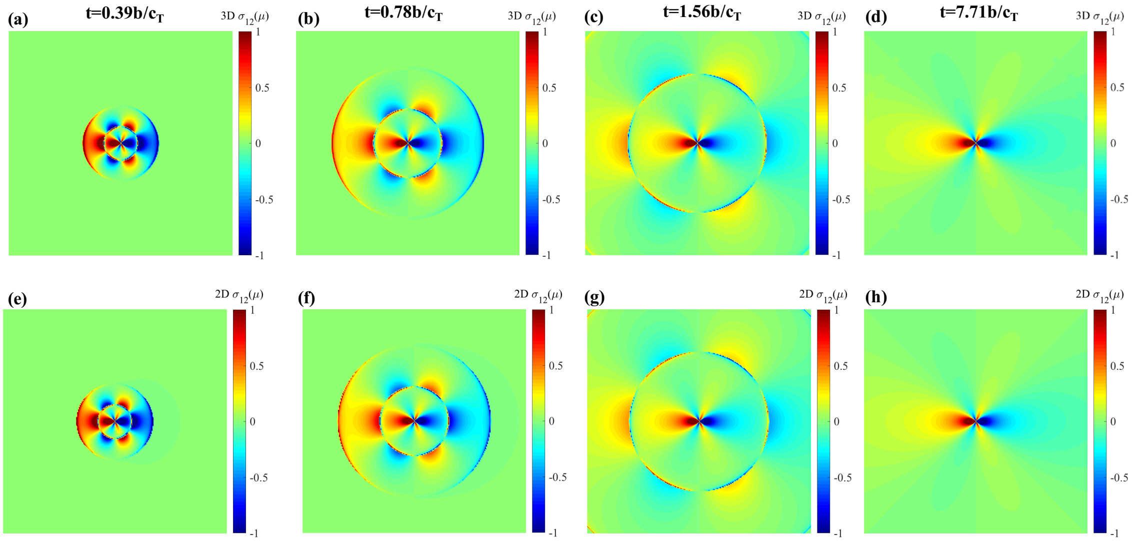

Figure 8: σ_{12} of an injected static edge dislocations on the plane GHIJ in Fig. 6 (a) (unit: μ), here $L_1 = L_2 = 2.5b$. (a-d) are obtained by our 3D-DDE, (e-h) are obtained by the 2D solution. The corresponding time t is marked above the figures.

In the following, the wave front singularity will be further analyzed to clarify its behavior. As discussed in section 5, the time-derivative terms play the dominant role for the singularity around the wave front. With respect to a static dislocation with $V = 0$, the second line $\mathbf{s}_{\text{line2}}(\mathbf{x}, t)$ and fourth line $\mathbf{s}_{\text{line4}}(\mathbf{x}, t)$ in Eq. (22) are the key terms. For a static straight edge dislocation with tangent direction along the x_3-direction and Burger's vector along the x_1-direction, these terms can be simplified as follows (see Appendix C for the derivation),

$$\begin{aligned}
&\mathbf{s}_{\text{line2}}(\mathbf{x},t) + \mathbf{s}^{\mathrm{T}}_{\text{line2}}(\mathbf{x},t)\\
&= -\partial_t \oint_{\mathcal{L}(t-R/c_{\mathrm{T}})} \frac{1}{c_{\mathrm{T}} R\,(R - \mathbf{R}\cdot\mathbf{V}/c_{\mathrm{T}})} \left(\frac{2\nu}{1-2\nu}\mathbf{b}\cdot(\mathbf{R}\times\boldsymbol{\xi})\mathbf{I} + \left(\mathbf{b} - \frac{2\mathbf{R}\cdot\mathbf{b}}{R^2}\mathbf{R}\right)\otimes(\mathbf{R}\times\boldsymbol{\xi}) + (\mathbf{R}\times\boldsymbol{\xi})\otimes\left(\mathbf{b} - \frac{2\mathbf{R}\cdot\mathbf{b}}{R^2}\mathbf{R}\right)\right) \mathrm{d}L' \\
&= -\frac{2b\mathrm{H}(c_{\mathrm{T}}t - l)}{c_{\mathrm{T}}t\sqrt{c_{\mathrm{T}}^2 t^2 - l^2}} \left(2R_2\left(\frac{1-\nu}{1-2\nu} - \frac{2R_1^2}{c_{\mathrm{T}}^2 t^2}\right)\mathbf{e}_1\mathbf{e}_1 + 2R_2\left(\frac{\nu}{1-2\nu} + \frac{2R_1^2}{c_{\mathrm{T}}^2 t^2}\right)\mathbf{e}_2\mathbf{e}_2 \right.\\
&\left. + \frac{2\nu R_2}{1-2\nu}\mathbf{e}_3\mathbf{e}_3 - R_1\left(1 + \frac{2(R_2^2 - R_1^2)}{c_{\mathrm{T}}^2 t^2}\right)(\mathbf{e}_1\mathbf{e}_2 + \mathbf{e}_2\mathbf{e}_1)\right)
\end{aligned} \tag{32}$$

$$\begin{aligned}
&\mathbf{s}_{\text{line4}}(\mathbf{x},t) + \mathbf{s}^{\mathrm{T}}_{\text{line4}}(\mathbf{x},t)\\
&= -\partial_t \oint_{\mathcal{L}(t-R/c_{\mathrm{L}})} \frac{1-2\nu}{(1-\nu)c_{\mathrm{L}} R\,(R - \mathbf{R}\cdot\mathbf{V}/c_{\mathrm{L}})} \left(\frac{\nu}{1-2\nu}(\mathbf{R}\otimes(\mathbf{b}\times\boldsymbol{\xi}) + (\mathbf{b}\times\boldsymbol{\xi})\otimes\mathbf{R}) - \frac{2\nu^2}{(1-2\nu)^2}\mathbf{b}\cdot(\mathbf{R}\times\boldsymbol{\xi})\mathbf{I} \right.\\
&\left. + \frac{\mathbf{R}\cdot\mathbf{b}}{R^2}(\mathbf{R}\otimes(\mathbf{R}\times\boldsymbol{\xi}) + (\mathbf{R}\times\boldsymbol{\xi})\otimes\mathbf{R})\right)\mathrm{d}L' \\
&= -\frac{2b(1-2\nu)\mathrm{H}(c_{\mathrm{L}}t - l)}{(1-\nu)c_{\mathrm{L}}t\sqrt{c_{\mathrm{L}}^2 t^2 - l^2}} \left(2R_2\left(\frac{-\nu^2}{(1-2\nu)^2} + \frac{R_1^2}{c_{\mathrm{L}}^2 t^2}\right)\mathbf{e}_1\mathbf{e}_1 - 2R_2\left(\frac{\nu(1-\nu)}{(1-2\nu)^2} + \frac{R_1^2}{c_{\mathrm{L}}^2 t^2}\right)\mathbf{e}_2\mathbf{e}_2 \right.\\
&\left. - \frac{2\nu^2 R_2}{(1-2\nu)^2}\mathbf{e}_3\mathbf{e}_3 + R_1\left(\frac{-\nu}{1-2\nu} + \frac{R_2^2 - R_1^2}{c_{\mathrm{L}}^2 t^2}\right)(\mathbf{e}_1\mathbf{e}_2 + \mathbf{e}_2\mathbf{e}_1)\right)
\end{aligned} \tag{33}$$

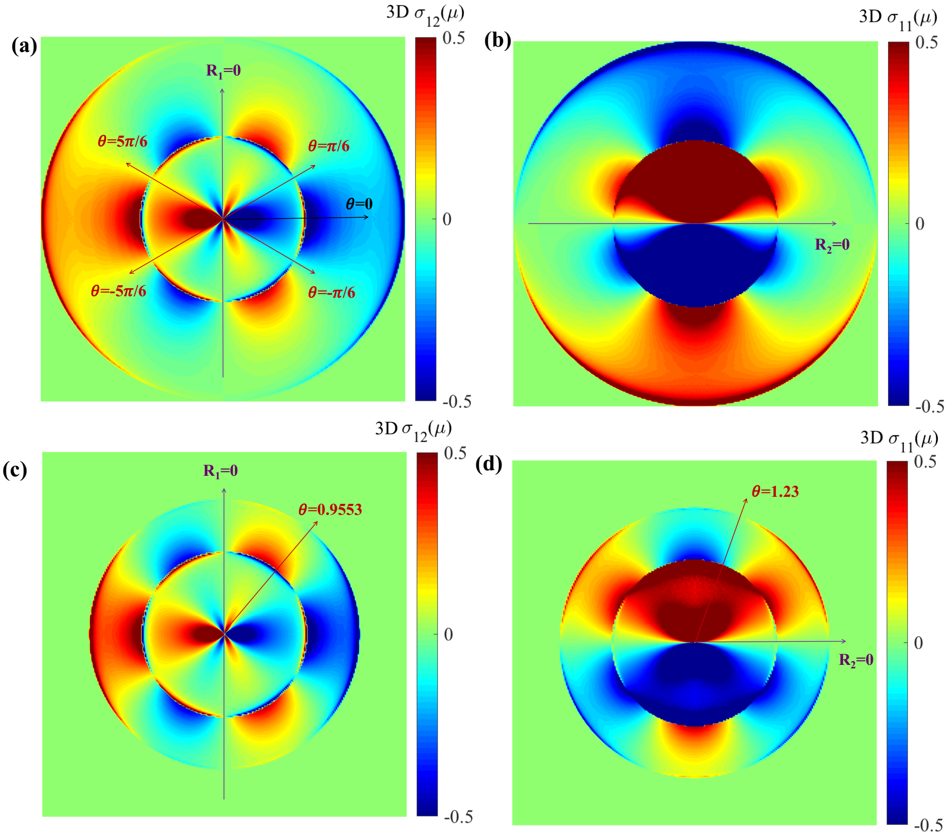

Figure 9: Stress field structure at the wave front for an injected static edge dislocations at $t = 1.136b/c_{\mathrm{T}}$, (a-b) $\nu = 0.3698$ (a) σ_{12} , (b) σ_{11}, (c-d) $\nu = 0.2$ (c) σ_{12} , (d) σ_{11}. Note that the stress threshold in this figure is different from Fig. D1 in order to clearly show the stress sign at the wave front.

where $\mathbf{e}_1$, $\mathbf{e}_2$, $\mathbf{e}_3$ are the base vectors of the coordinate system. The quantities R_i (i=1,2,3) are the components of $\mathbf{R}$ in the considered coordinate system. Eqs. (32) and (33) are useful in predicting the angular dependence of the wave front singularity for a static straight edge dislocation. The basic idea is that the singularity around the transverse and longitudinal wave fronts disappears, when the corresponding coefficients in Eq. (32) and Eq. (33) are zero, respectively. For instance, taking σ_{12} at transverse wave front, this means that $R_1\left(1+\frac{2(R_2^2-R_1^2)}{c_T^2t^2}\right)=0$ according to Eq. (32). If the field point is on a plane with $x_3=0$, at the wave front, $R_2=c_Tt\sin\theta$, $R_1=c_Tt\cos\theta$, so $R_1\left(1+\frac{2(R_2^2-R_1^2)}{c_T^2t^2}\right)=0$ means that $R_1=0$ or $\sin^2\theta=1/4$. Here, θ is the angle from the direction connecting field point and dislocation and the x_1 direction on the x_1x_2 plane, as indicated in Fig. 9. Therefore, in Fig. 9(a), at the transverse wave front, the singularity disappears when $R_1=0$, or $\theta=\pm\pi/6, \pm 5\pi/6$. Similarly, for σ_{12} at the longitudinal wave front, one can find that the singularity disappears when $R_1=0$ or $\cos^2\theta=\frac{1-3\nu}{2(1-2\nu)}$. Only when $\nu<1/3$, there is a solution for θ. For the considered material parameters, there is no solution for θ. Therefore, only when $R_1=0$, the singularity disappears at the longitudinal wave front, as clearly shown in Fig. 9(a). To demonstrate the effect of Poisson's ration ν, we recalculate the same problem but use $\nu=0.2$. Then, according to the condition: $\cos^2\theta=\frac{1-3\nu}{2(1-2\nu)}$, when $\theta=0.9553$, the singularity of σ_{12} at the longitudinal wave front circle disappears, which is exactly reflected in Fig. 9(c).

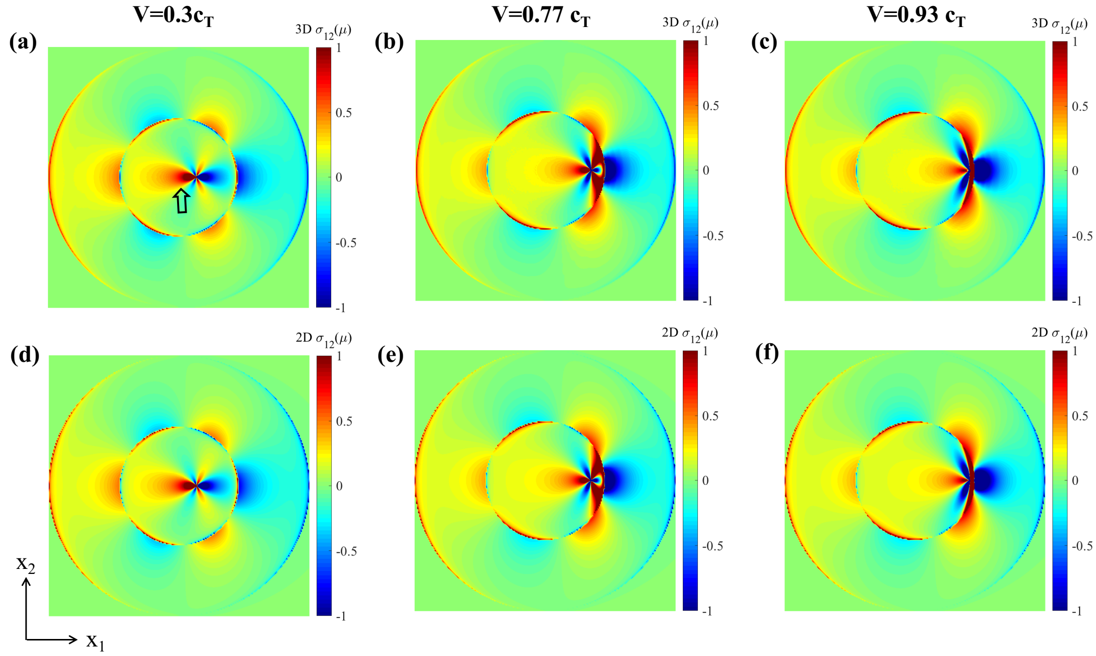

Figure 10: σ_{12} of a uniformly moving edge dislocations on plane GHIJ in Fig. 6(a) (unit: μ), here $L_1=L_3=2.5b$, $t=1.136b/c_T$. (a-c) 3D DDE results, (d-f) are 2D solution. The corresponding dislocation velocity is marked on the top.

In addition, one notices that decreasing ν leads to lower c_L, and therefore to a smaller longitudinal wave front circle. Similarly, we can also discuss the singularity of σ_{11} at the longitudinal wave front according to Eq.(33). One can find that the singularity disappears when $R_2=0$ or $\cos^2\theta=\frac{\nu^2}{(1-2\nu)^2}$. Therefore, θ only exists when $\nu<1/3$. When ν=0.3698, there is no solution, which is consistent with the observation in Fig. 9 (b) that the longitudinal wave front singularity only disappears when $R_2=0$. In contrast, when ν=0.2, the longitudinal wave front singularity also disappears for $\theta=1.23$, as shown in Fig. 9 (d). The discussion above demonstrates that the value of ν has a strong influence on the wave front singularity.

4.3. Uniform Motion of a Straight Edge Dislocation

In this section, the stress field induced by a moving straight edge dislocation line is studied. Here, the dislocation line shown in Fig. 6(a) moves along the x_1-direction, with a velocity magnitude v. Fig. 10 gives the stress field induced by injected uniformly moving dislocation at three different velocities, $V = 0.3c_{\mathrm{T}}$, $0.77c_{\mathrm{T}}$, and $0.93c_{\mathrm{T}}$, but at the same time $t = 1.136b/c_{\mathrm{T}}$. With the increase of the velocity, the stress field map is significantly different around the dislocation core region. For high velocity, the high shear stress region around x_2 direction expands. In contrast, the positive shear stress stress region along the x_1 direction (see the red region indicated by arrow in Fig. 10(a)) gradually shrinks with increasing velocity. The calculation results are compared with the corresponding 2D solution, and good consistency is observed. Consistent results are also obtained for the stress field of a uniformly moving dislocation with velocity $0.8c_{\mathrm{T}}$ from static rest conditions (i.e. the dislocation existed at initial time and not injected as in the previous case), as shown in Fig. D2 .

4.4. Motion of a Straight Screw Dislocation

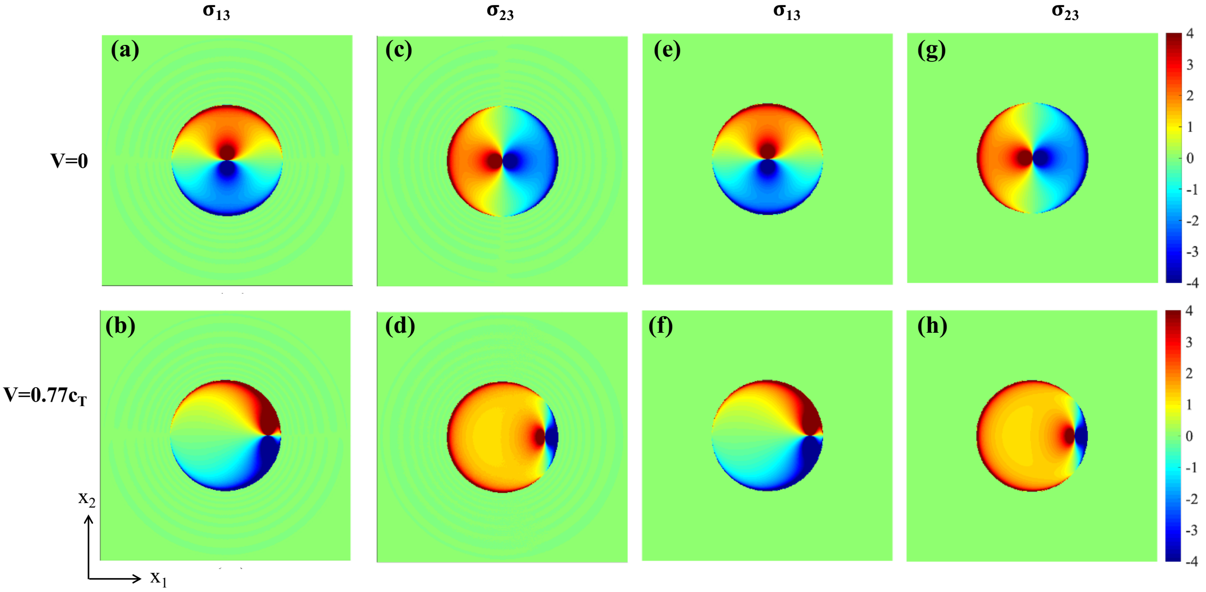

Figure 11: Stress field (unit: $10^{-4}\mu$) of screw dislocation in x_1x_2 plane, with $L_1 = L_2$=2.1 μm, $t = 0.15$ ns. (a-d) 3D-DDE calculation result, (e-h) Analytical solution by Eq. (34)

After verifying the accuracy of the stress field calculations for the 2D edge dislocation, we further check the results of a screw dislocation. Consider now an injected infinitely-long screw dislocation, as described by Fig. 6 (a). The dislocation line and Burger's vector direction are along x_3, and the dislocation line has a constant velocity V along the x_1-direction. The stress field at a field point $(x_1, x_2, 0)$ has an analytical solution,

$$\begin{aligned}\sigma_{13} &= \frac{\mu b x_2}{2\pi\sqrt{t^2 - l^2/c_{\mathrm{T}}^2}}\,\frac{-t + x_1 v/c_{\mathrm{T}}^2}{l^2 - 2x_1 t v - x_2^2 v^2/c_{\mathrm{T}}^2 + v^2 t^2}\mathrm{H}(t - l/c),\\ \sigma_{23} &= \frac{\mu b}{2\pi\sqrt{t^2 - l^2/c_{\mathrm{T}}^2}}\,\frac{x_1 t - x_1^2 v/c_{\mathrm{T}}^2 - t^2 v + t x_1 v^2/c_{\mathrm{T}}^2}{l^2 - 2x_1 t v - x_2^2 v^2/c_{\mathrm{T}}^2 + v^2 t^2}\mathrm{H}(t - l/c),\end{aligned} \tag{34}$$

where $l^2 = x_1^2 + x_2^2$. This solution is derived by using the results given in (Gurrutxaga-Lerma et al., 2015b), and is used for benchmarking the numerical implementation. The calculation results by 3D DDE at $t = 0.15$ ns are given in Fig. 11 (a-d), which are consistent with the analytical solution given in Fig. 11 (e-h). Comparing Fig.11 (a) and (b), when the dislocation motion velocity changes from 0 to $0.77c_{\mathrm{T}}$, the stress field map changes significantly. However, in both cases, the stress field is only within the region that the transverse wave can reach. This is significantly different from the results of the edge dislocation, such as shown in Fig. 10 (b), where the two-wave structure is observed.

We further consider an accelerated screw dislocation and compare its near-field stress field with the singular asymptotic solutions given in (Callias and Markenscoff, 1988). We aim to demonstrate that our method can capture the logarithmic singularity with a coefficient proportional to acceleration and $(1 - V^2/c_T^2)^{-3/2}$. Fig. 12 (a) gives the stress field distribution of an accelerated screw dislocation, which has a constant acceleration $a = [4 \times 10^{-5} c_T^2/b \quad 0 \quad 0]$, and its velocity magnitude increases from 0 to $0.77c_T$. In order to analyze the near-field singularity, we investigate the stress value at a small distance ϵ away from the current dislocation line, as shown in Fig. 12 (a). We considered a screw dislocation accelerated from 0 to $0.77c_T$ with several different accelerations (a, $a/2$, $a/4$), and calculated the difference of their corresponding stress value along ϵ. Calculating the stress difference with the same current velocity and different accelerations separates out the logarithmic singularity, because the $1/\epsilon$ singularity depends on the current velocity and not on the acceleration. As shown in Fig. 12 (b), the linear-type curve in the semi-logarithm plot illustrates that there is a logarithmic singularity. In addition, if the logarithmic singularity has a coefficient proportional to acceleration, the shear stress difference $\sigma_{23}(a) - \sigma_{23}(a/2) \propto (a - a/2)\ln(\epsilon)$ and $\sigma_{23}(a) - \sigma_{23}(a/4) \propto (a - a/4)\ln(\epsilon)$, so $\sigma_{23}(a) - \sigma_{23}(a/2)$ should be equal to $2/3(\sigma_{23}(a) - \sigma_{23}(a/4))$. This is successfully captured in Fig. 12 (b). Furthermore, if the logarithmic singularity has a coefficient proportional to $(1 - V^2/c_T^2)^{-3/2}$, $(\sigma_{23}(a) - \sigma_{23}(a/2))(1 - V^2/c_T^2)^{3/2}$ should have the same slope, when the accelerated screw dislocation reaches different current velocities. This prediction is reproduced in Fig. 12 (c). Therefore, our calculations are consistent with previous theoretical predictions performed by Callias and Markenscoff (1988).

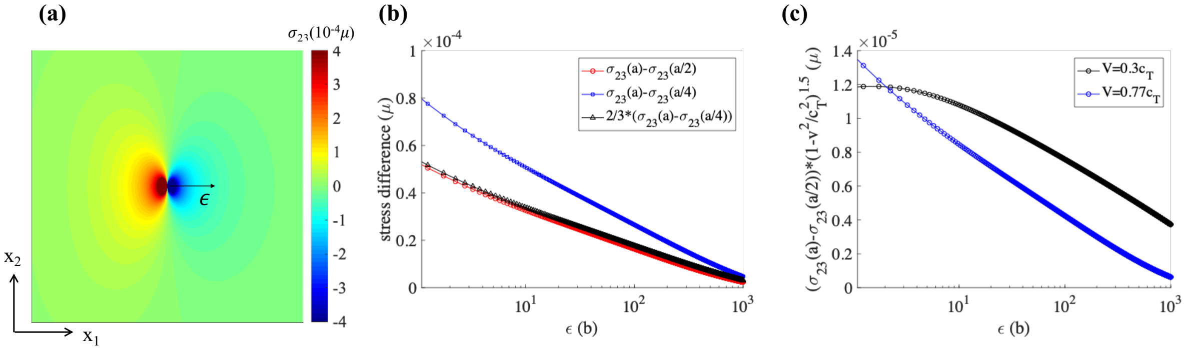

Figure 12: (a) Stress field of an accelerated screw dislocation on the x_1x_2 plane, with $L_1 = L_2$=2.1 μm. (b) Stress difference of screw dislocation with the same current velocity $0.77c_t$ but different accelerations (a, $a/2$, and $a/4$). Here, $a = [4 \times 10^{-5} c_T^2/b \quad 0 \quad 0]$. ϵ is defined as shown in (a). (c) Stress difference of accelerated screw dislocation with various current velocities V.

5. New Insights on Elastodynamic Effects

In this section, we will present new results for 3D dislocations that cannot be fully obtained through 2D calculations. The moving shear dislocation loop is taken as an example of a prototypical 3D dislocation, which, once established, can be used in future full-fledged 3D DDE simulations. The elastodynamic stress field of a moving shear loop and the interaction forces between two shear dislocation loops will be presented and discussed for the first time.

5.1. Stress field of a moving shear dislocation loop

Section 4 clearly demonstrates that the stress field of a straight dislocation strongly depends on its motion history, and is that it is significantly different from the quasi-static stress field. Therefore, the stress field of a moving dislocation loop is also expected to deviate significantly from its quasi-static counterpart. To reveal such difference, we design here several cases. All considered dislocation loops move to reach a final radius of 100b. To clearly show the stress field of the moving shear loop, the results on three cut-planes (x_1x_3, x_1x_2, and x_2x_3) will be presented. All these cut planes have the size (410×410) b.

Case 1- The expanding shear loop: A shear dislocation loop is assumed to have an initial radius of 1b, which may represent a nucleated embryo, or generated due to irradiation or dislocation interactions. This hypothetical loop lies on the x_1x_3-plane, with its center situated at $[0 \quad 0 \quad 0]$. Its Burger's vector is along [100], so the normal direction of its glide plane is [010]. The loop expands outwards to reach a final radius of 100b with uniform velocity, varied at $0.3c_{\mathrm{T}}$, $0.6c_{\mathrm{T}}$, and $0.9c_{\mathrm{T}}$, respectively. Therefore, the total motion duration of the dislocation loops with a higher velocity is shorter. In the results presented below, it is easier to observe the wave front for the higher-velocity case, since the shorter time may not be sufficient to make the wave front fully develop in our computational domain.

From Fig. 13 (a-d), one notices that with the increase in the loop expansion velocity, the positive stress region (red region around the dislocation loop) around the screw part of the shear loop shrinks significantly. This is easy to be understood, because the stress field of an injected pure edge dislocation can reach the region where the longitudinal elastic waves can reach, but the stress field of injected pure screw dislocation can only reach the region where the transverse elastic waves arrive. For the high velocity case, the total motion duration is short, so the difference between the edge and screw regions is more obvious. From Fig. 13 (e-h), the velocity effect on the stress field map is very similar to the trend observed in Fig. 10. This is because the intersection part of the shear dislocation loop with the x_1x_2-plane is of an edge character, so the stress field map shown in Fig. 13 (e-h) is similar to the superposition of the stress field σ_{12} induced by two straight edge dislocations with opposite signs and direction of motion (i.e. an expanding edge dipole). As an example, the stress field map on the x_1x_2-plane of a dislocation loop and the corresponding two straight edge dislocations are compared in Fig. 13 (h) and Fig. 14 (a). Some similarity is observed. However, it can be seen that the wave-front singularity of this expanding dislocation loop is much weaker as compared to that for two straight dislocation lines. This can be understood as follows. According to the discussion in section 3.3, the wave front singularity is mainly dominated by the time derivative terms. The retarded dislocation corresponding to the field point on the wave front generally corresponds to the initial dislocation position. Since the initial dislocation loop is very small (with radius 1b), it is natural to expect that the change of the stress field at the wave front induced by such small loop is also small. Therefore, the wave front singularity for the expanding loop is weaker. In addition, a comparison between Fig. 13 (h) and Fig. 14 (a) also demonstrates other differences induced by the loop curvature. For example, a larger negative stress field region is observed inside the loop in Fig. 13 (h). From Fig. 13 (i-l), with the increase of the velocity, the red positive stress region is significantly compressed. Because the corresponding intersection part of the loop with the cut plane is of a screw character, the stress field in Fig. 13 (i-l) is similar to the superposition of the stress field induced by two straight screw dislocations with opposite sign and opposite direction of motion, i.e., an expanding screw dipole (see Fig. 11 (c) and (d)). However, in Fig. 13 (i-l), the negative stress is less compressed due to the curvature effect, compared with Fig. 11 (d).

Case 2- The small contracting shear loop:

If the shear loop shrinks instead of expands, its stress field may exhibit different features. To check this possibility, we first consider the case that the initial dislocation loop is static and has a radius of 200b. The contraction velocity is varied as $-0.3c_{\mathrm{T}}$, $-0.6c_{\mathrm{T}}$, and $-0.9c_{\mathrm{T}}$. Here, the negative sign represents contracting direction towards the center of the loop. Therefore, when this loop finally shrinks to reach a radius of 100b, its motion duration is similar to Case 1. The slip plane and Burger's vector are the same as in Case 1.

The corresponding stress fields are presented in Fig. 15, where it is clear that the stress field map is different from the results of the expanding loop in Fig. 13, especially for the high velocity case. This is mainly because the retarded dislocation configurations are significantly different for the expanding loop in Case 1 and the contracting loop in Case 2. One example is shown in Fig. 16 (a) and (b). Here, the retarded positions corresponding to the field point $(100b, 0, 0)$ are plotted. One notices that the higher the velocity, the more significant the difference in the shape of the retarded dislocation corresponding to the expanding loop and contracting loops. Moreover, for the contracting loop from 200b to 100b, when the velocity is $-0.6c_{\mathrm{T}}$ or $-0.9c_{\mathrm{T}}$, a large part of the retarded dislocation actually corresponds to the initial static loop. Therefore, the stress field in Fig. 13 is indeed a superposition of the stress field induced by some part of initial static loop, and some part of moving loop when V is $-0.6c_{\mathrm{T}}$ or $-0.9c_{\mathrm{T}}$.

Since the motion duration is not long enough to allow the elastic wave front to move out of the simulation domain, the wave front singularity is observed from Fig. 15. As discussed earlier, the stress field map in Fig. 15 (d-f) shares some features with those of two straight edge dislocations in a dipole configuration. The wave front singularity of the expanding loop in Fig. 13 is found to be weaker than that of the two corresponding edge dislocations, however. In contrast, it is found that the wave front singularity of the contracting loops observed in Fig. 15 is even stronger, compared with their edge dislocation dipole counterpart. To illustrate this feature, Fig. 14 (b) shows the corresponding stress field of two straight edge dislocation lines. They initially have a distance of 400b along x_1 direction, and then move towards each other with velocity magnitude $0.9c_{\mathrm{T}}$ until their distance is 200b. Obviously, the longitudinal wave front singularity in Fig. 15 (f) is more significant than that in Fig. 14 (b). This can also be easily understood by our

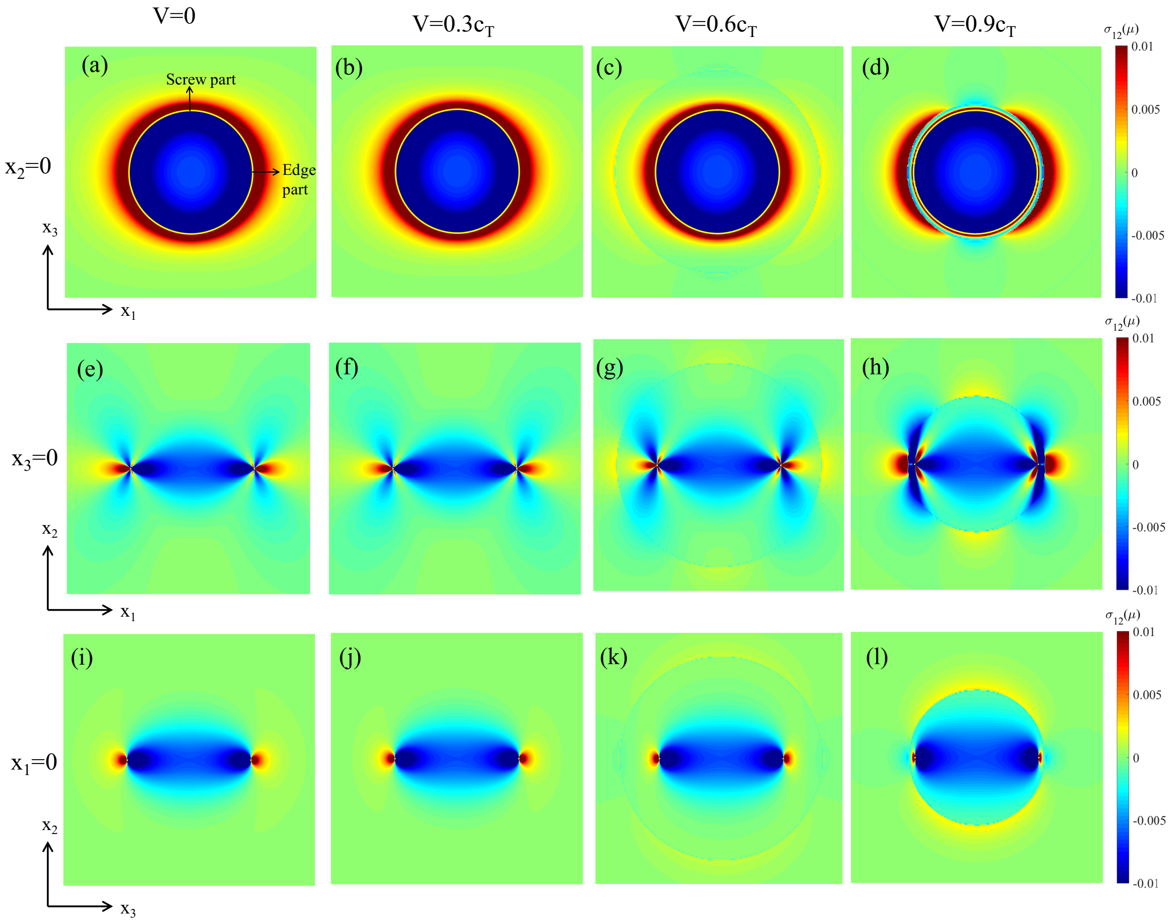

Figure 13: Stress field σ_{12} (unit: μ) of a uniformly expanding dislocation loop with initial radius 1b and final radius 100b. The yellow solid line in (a-d) is added to show the position of the current dislocation loop

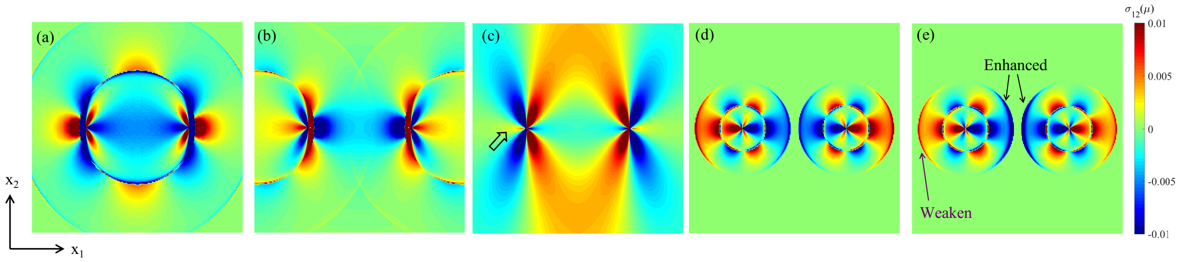

Figure 14: Stress field σ_{12} on the x_1x_2-plane (410 × 410)b (a-d) two straight edge dislocations with opposite line directions along the x_3-axis, and (e) an injected static shear dislocation loop. (a) Two injected straight dislocations, which have an initial distance 2b, then move away from each other with speed $0.9c_{\mathrm{T}}$ along the x_1-direction until their distance becomes 200b. (b) Two static straight dislocations, which have an initial distance of 400b, move towards each other with the speed $0.9c_{\mathrm{T}}$ along the x_1-direction until their distance becomes 200b. (c) Two static straight dislocations, which have an initial distance 8000b, move towards each other with speed $0.9c_{\mathrm{T}}$ along x_1 direction until their distance become 200b. (d) two injected static straight dislocation with separation distance 200b when the current time is $t = 45b/c_{\mathrm{T}}$. (f) one injected static loop with radius 100b when $t = 45b/c_{\mathrm{T}}$

finding that the wave front singularity is associated with the time derivative terms in the stress field equations. For the wave front field point with coordinates $(x_1, x_2, 0)$ in x_1x_2 plane, if the absolute value of x_1 is smaller than the current

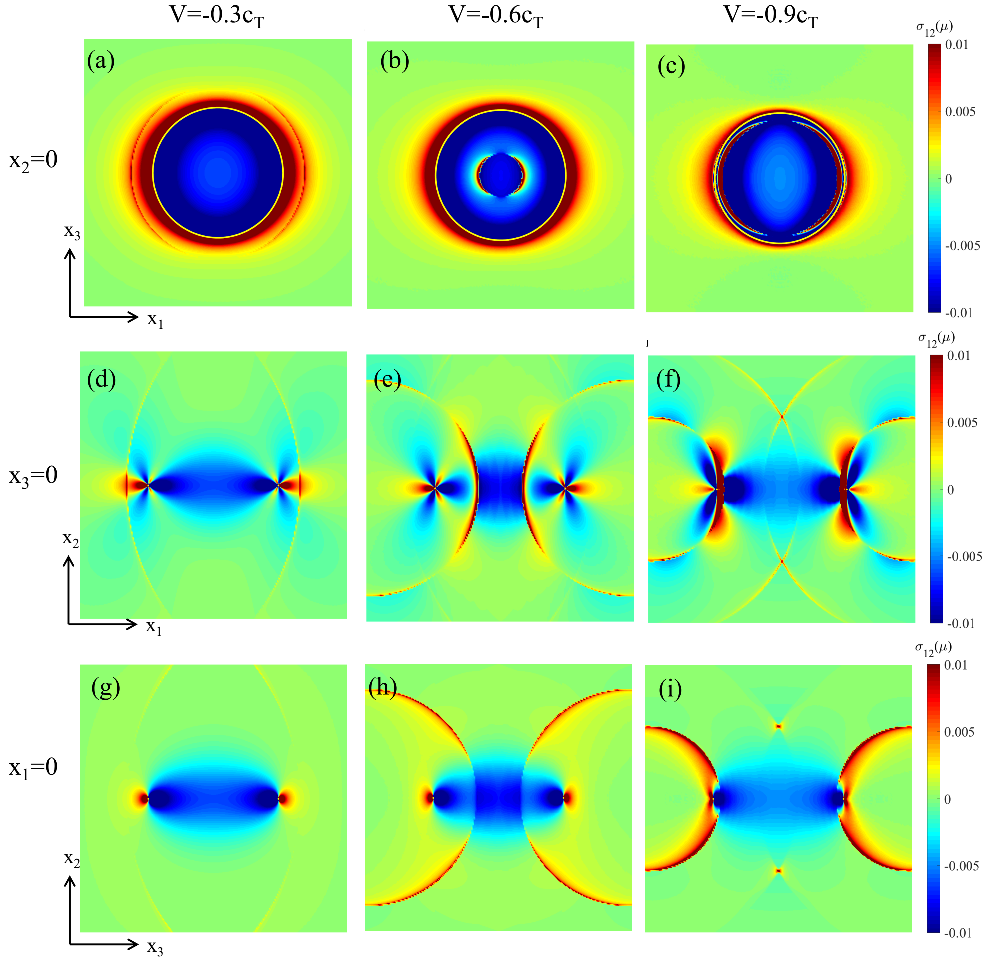

Figure 15: Stress field σ_{12} of a uniformly-contracting dislocation loop with initial radius of 200b and final radius of 100b. The yellow solid line in (a-c) is added to show the current position of the loop.

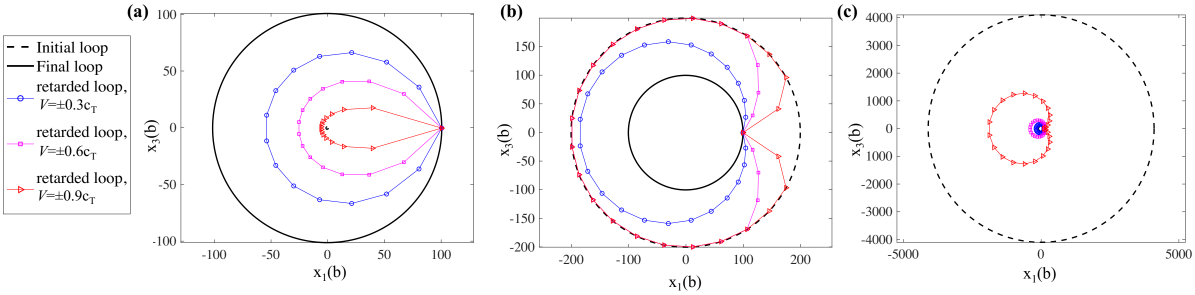

Figure 16: Retarded dislocation loop shape corresponding to the field point $(100b, 0, 0)$ of (a) an expanding dislocation loop with radius from 1b to 100b, (b) a contracting dislocation loop with radius from 200b to 100b, (c) a contracting dislocation loop with radius from 4000b to 100b

loop radius, more retarded points can be found for these field points due to the curvature effect, compared with those for two straight edge dislocation lines, so it is more possible that the corresponding time derivative terms are larger. For the field points in the other region, if less retarded points are found, the time derivative terms should be weaker. To verify this hypothesis, we compare the stress field induced by an injected static shear loop and two static straight edge dislocation lines, at time $t = 45b/c_\mathrm{T}$. As expected, the wave front singularity is enhanced in the middle region, but is weakened in the other region, as shown in Fig. 14 (d-e).

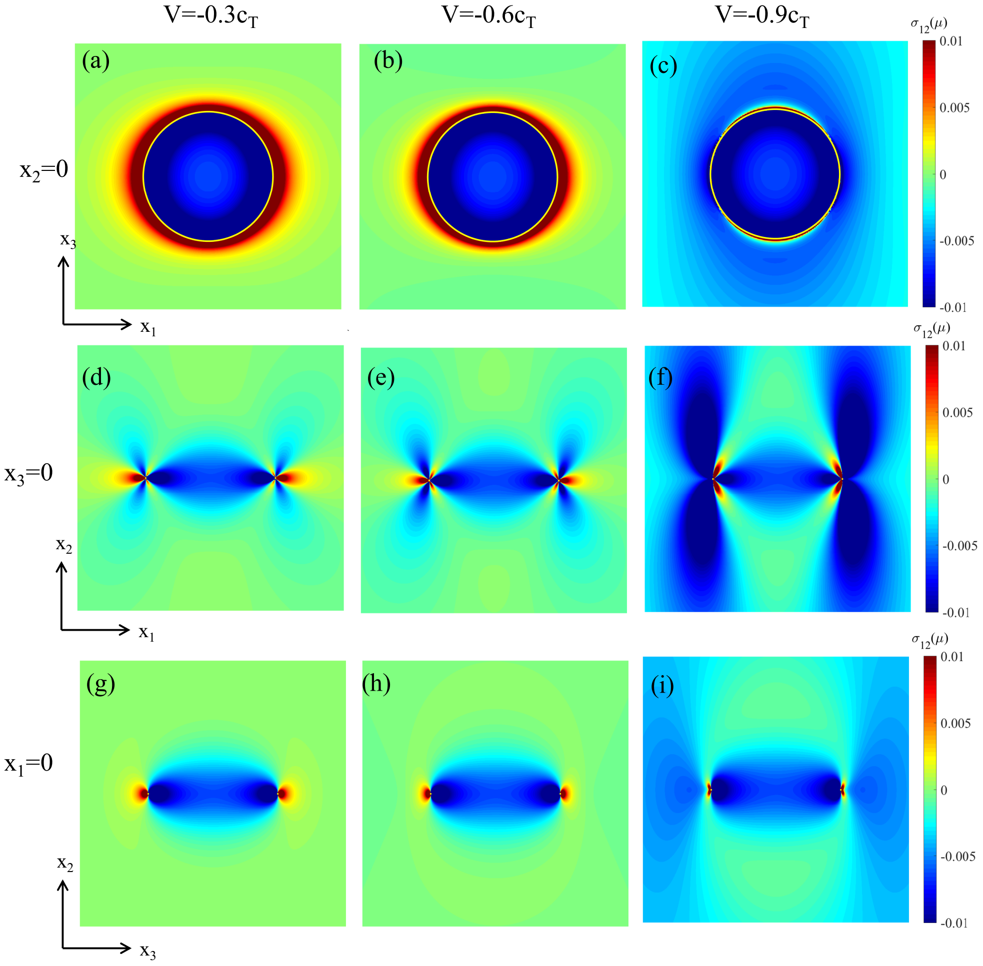

Figure 17: Stress field σ_{12} of a uniformly contracting dislocation loop with initial radius of 4000b and final radius 100b. The yellow solid line in (a-c) is added to show the current position of the dislocation loop.

Case 3- The large contracting shear loop: To avoid the influence of wave front on the stress field map of a contracting shear loop, we further consider the contraction process of a large loop with an initial radius of 4000b. All other conditions are the same as in Case 2. For the computational domain of $(410 \times 410 \times 410)$b, the retarded dislocation loops all correspond to the moving dislocation, instead of partly containing the contribution of the initial static dislocations as in Case 2. One example of the retarded dislocation corresponding to the field point $(100b, 0, 0)$ is shown in Fig. 16(c).

Figure 17 shows the corresponding stress field for Case 3. When the contraction velocity is $-0.3c_\mathrm{T}$ and $-0.6c_\mathrm{T}$, the stress distributions on the three cut planes are similar to those for the expanding loop in Fig. 13. This means that even though their retarded dislocation shapes are different at low velocity, the influence on the stress field map is not noticeable. Similar behavior is also observed for the straight edge dislocation. When the wave front is far away from the field point region, the stress field of the pure edge dislocation with steady velocity of opposite sign is also similar.

However, at the high velocity of $-0.9c_{\mathrm{T}}$, there is a big difference between the stress field of the expanding loop and contracting loop. In addition to their significantly different retarded dislocation configurations, the expanding loop in Fig. 13 (d,h,l) is also strongly influenced by the wave front, but the wave front has a weak effect on the contracting loop in Fig.17 (c,f,i).

It is found, e.g., by comparing the stress field maps on the x_1x_2-plane of Figs. 17(f) and 14(c), that as time flows the difference gets larger between the shear loops and the straight edge dislocation dipole, which is an effect of loop curvature. Another interesting point relates to the observation that the positive shear stress region along the x_1 axis completely disappears for an infinite straight edge dislocation moving steadily at a velocity V larger than the Rayleigh wave speed c_{R} (Hirth and Lothe, 1982), which acts as a threshold for this effect. Here, $c_{\mathrm{R}} = 0.94c\mathrm{T}$ with the material parameters considered. For a loop, the positive stress zone marked out by an arrow in Fig. 14(c) is absent in Fig. 17(f), which suggests that this threshold is lowered by curvature.

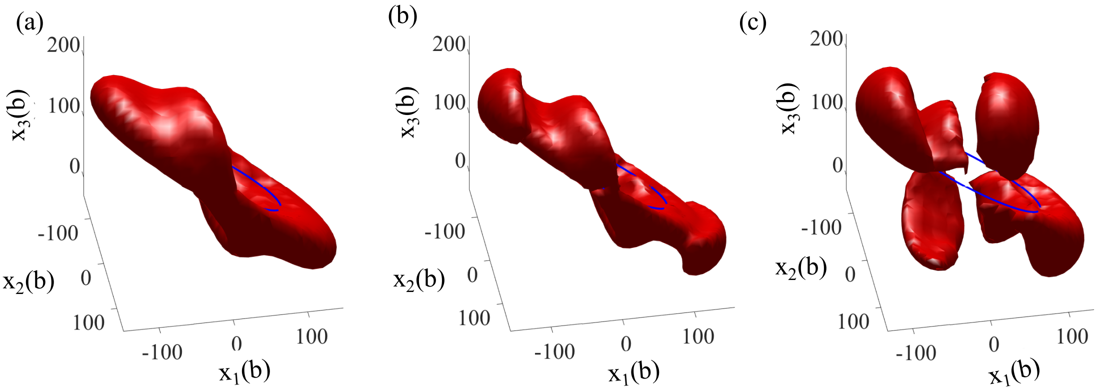

Figure 18: Normal stress isosurface $\sigma_{11} = 10^{-3}\mu$ in the local loop coordinates. The shear loop expands with velocity (a) $V = 0.3c_{\mathrm{T}}$, (b) $V = 0.6c_{\mathrm{T}}$, (c) $V = 0.9c_{\mathrm{T}}$. The solid blue line represents the dislocation loop

Case 4- Oblique shear loop: We consider here an oblique loop oriented on the slip plane $(1\bar{1}1)$. Its Burger's vector is $[\bar{1}10]$. The loop has an initial radius of 1b, and moves with uniform velocity to a final radius of 100b. Representative velocities are $0.3c_{\mathrm{T}}$, $0.6c_{\mathrm{T}}$, $0.9c_{\mathrm{T}}$, respectively. Fig. 18 shows an isosurface for the normal stress $\sigma_{11} = 10^{-3}\mu$ in the vicinity of the shear loop. The normal stress isosurface is symmetric with respect to the loop center. As the loop expansion velocity increases, the elastic wave front is more clearly observed in the structure of the stress isosurface. In addition, the positive normal stress gradually disappears around the screw part of the shear loop, which is consistent with the discussion presented in Case 1 (see Fig. 13(a-d)). The structure of the isosurface at low speeds (Fig. 18 (a)) is the same as our earlier calculations for a static loop (Ghoniem and Sun, 1999)-Fig. 4, while it is completely different at high speeds (Fig. 18 (c)).

Case 5- Expanding shear loop with acceleration: We consider an accelerated dislocation loop and compare its near-field stress around the screw part with the singular asymptotic solutions given in (Markenscoff and Ni, 1990). The aim here is to demonstrate that in addition to logarithmic singularity with a coefficient proportional to the acceleration and $(1 - V^2/c_T^2)^{-3/2}$, there is an additional logarithmic singularity for a loop with a coefficient proportional to $1/r_l$. Here, r_l is the curvature radius of the loop. The set-up is similar to Case 1, except that the loop expands outwards from zero velocity to reach a final velocity of $0.6c_T$ with a constant acceleration along the radial direction and magnitude $|a| = 1.8 \times 10^{-4}c_T^2/b$. The radius of the loop increases by 1000b. Fig. 19 (a) shows the stress field distribution around the screw part of the loop. To investigate the effect of the curvature radius, we consider various initial loop radii (1b,1000b, 2000b). Their corresponding final radius is 1001b, 2000b, and 3000b, which are expressed as r_l, $2r_l$, and $3r_l$, respectively in Fig. 19 (b). As demonstrated in Fig. 19 (b), the linear curve in the semi-logarithm plot illustrates that there is logarithmic singularity. In addition, $\sigma_{12}(r_l) - \sigma_{12}(2r_l)$ is equal to $3/4(\sigma_{12}(r_l) - \sigma_{12}(3r_l))$, which is consistent with the prediction given by (Markenscoff and Ni, 1990) that the coefficient of one logarithmic singularity is proportional to $1/r_l$.

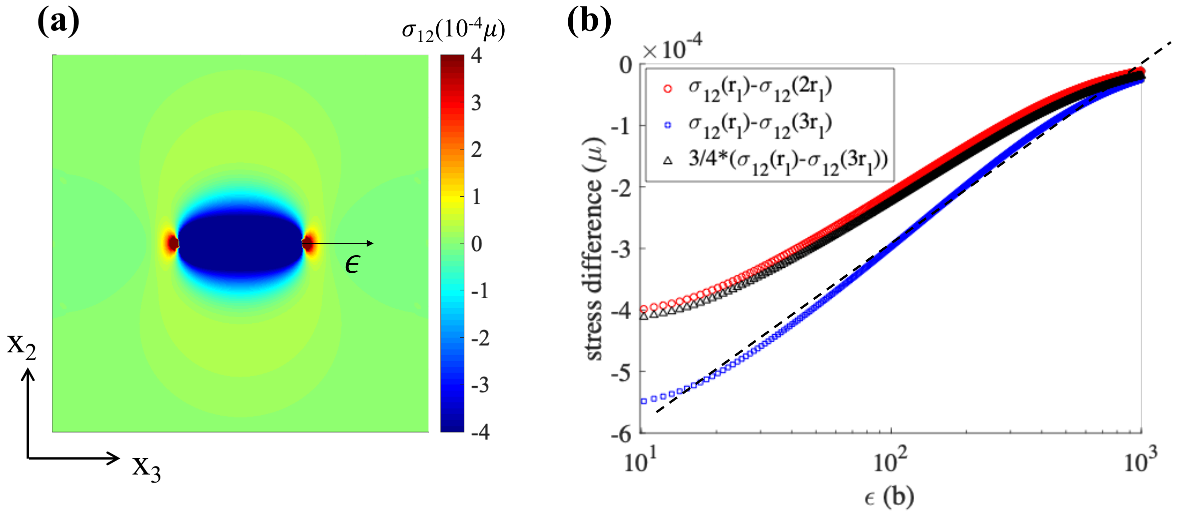

Figure 19: (a) Stress field σ_{12} of an accelerated expanding dislocation loop with initial radius 1b and final radius 1001b. The cut plane has the size of 3000 × 3000b. (b) Stress difference of the screw part of the loop with the same acceleration $|a| = 1.8^{-4} c_T^2/b$ and current velocity $0.6c_t$ but different final radius (r_l, $2r_l$, and $3r_l$). ϵ is defined as shown in (a).

5.2. *Interaction between shear dislocation loops*

Section 5.1 demonstrates that the stress field of moving shear dislocation loop deviates from the static pattern in a rather remarkable way. The spatial structure of the field is strongly dependent on the time of motion and the dislocation speed. In DDD simulations, the reactions between dislocations (i.e. junction formation/ breakup, cross-slip, force transfer, etc.) are all driven by the PK configurational force (PK-force for short). Since the PK-force is dictated by the field of neighboring dislocations and the applied external field, many interesting results may be expected for dynamically-interacting neighboring dislocations. In this section, we use a simple case to illustrate such purely elastodynamic effects, which may be useful in future full-fledged DDE simulations. Close to the moving shear loop, we place another shear dislocation loop #2 on a parallel slip plane with an offset distance of 5b along the x_2 direction. The shear loop #2 has the same Burger's vector and slip plane as the moving shear loop, but has an opposite tangent direction. We consider different radii of loop #2: 50b, 100b, and 120b, respectively, and calculate the PK-force along on loop #2 induced by the moving shear loop.

Fig. 20 shows the PK-force along the loop #2 induced by expanding and contracting shear loop #1 with velocity $\pm 0.3c_T$, $\pm 0.6c_T$, $\pm 0.9c_T$, respectively, corresponding to Case 1 and Case 3 in section 5.1. In Fig. 20, the arrows with color, red or blue, respectively, indicate the expansion or contraction force along the radius direction. The magnitude of the arrow is proportional to the force magnitude, and hence can be taken as a rough estimate for the deformed shape of the loop. If the static stress approximation is used, the PK-force on loop #2 is similar to Fig. 20 (a), which does not depend on the dislocation motion history. However, the actual elastodynamic stress field leads to strong dependence of the PK-force on the dislocation history. From Fig. 20, when the radius of the loop #2 (50b) is much smaller than that of the moving shear loop #1, the PK-force is not very sensitive to the velocity of motion. However, when loop #2 has the same or similar radius (100*b* or 120*b*) compared with the final radius of the moving shear loop, the PK-force magnitude changes considerably, as the magnitude of the velocity increases. More interestingly, the sign of the PK force also partly changes with the increase of velocity. Simple calculations indicate that the PK-force on the slip plane is proportional to $-\sigma_{12}$. Therefore, the change of the magnitude and sign of the PK-force along loop #2 can be easily understood through changes in the corresponding stress field $-\sigma_{12}$ on the x_1x_3-plane, and x_2=5b, as shown in Fig. 21. The position of Loops #2 is plotted as white dotted lines in Fig. 21 for visualization. Fig. 21 share many common features with Fig. 13(b-d) and Fig. 17(a-c), with respect to the velocity effect on the stress field map. This example shown in Fig. 20 clearly demonstrates that the elastodynamic stress field of a moving dislocation loop will significantly change all short-range dislocation interactions. Two neighboring shear loops may be attracted in the static case to form a tight dipole, but may repel each other if the elastodynamic effect is taken into account, such

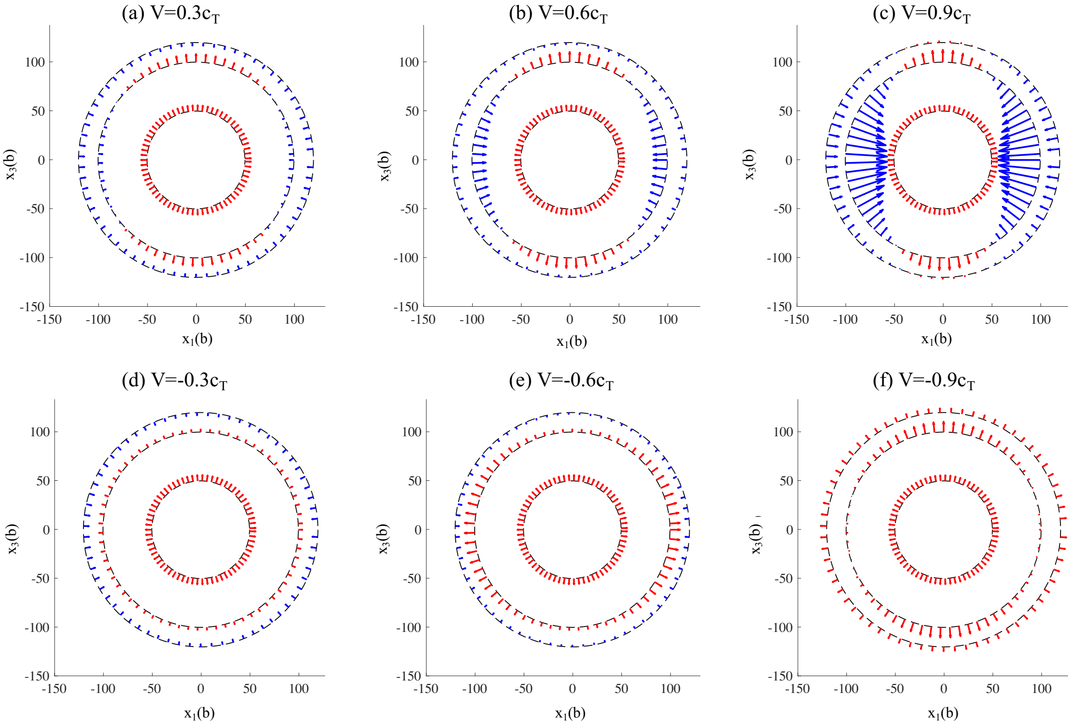

Figure 20: PK force on a shear dislocation loop #2 induced by a neighboring high-speed dislocation loop. In each figure, results of three different radii of loop #2 (50b, 100b, 120b) are shown. (a-c) The source shear loop expands with velocity $0.3c_T$, $0.6c_T$, $0.9c_T$, respectively. (d-e) The source shear loop contracts from 4000b radius to 100b radius with velocity $-0.3c_T$, $-0.6c_T$, $-0.9c_T$, respectively. Red arrows are along the direction away from the center of the loop, while the blue arrows are towards the loop center. The magnitude of the PK-force is proportional to the length of the arrows.

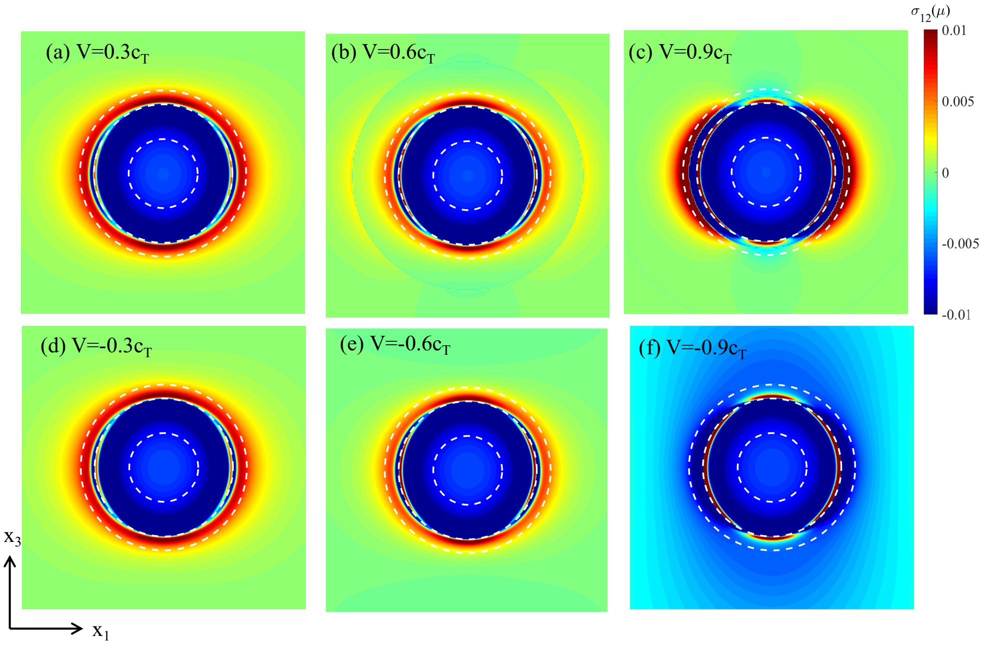

Figure 21: Shear stress σ_{12} distribution induced by a moving shear loop of Case 1 and Case 3, whose velocity is marked on the figures. The white dotted lines correspond to the field dislocation loop #2 in Fig. 20.

as Loop#2 with radius 120b in Fig. 20(f). Moreover, expanding loop and contracting loops may also lead to even different signs of the interaction force, such as shown in Fig. 20 (c) and (f).

6. Conclusions

The significant effects of elastodynamics on dislocation stress field have been recognized for a long time (Eshelby, 1949; Lazar and Pellegrini, 2016; Markenscoff and Clifton, 1981; Mura, 1963). However, till now, understanding the elastodynamic effects on fundamental dislocation behavior and interactions theoretically or computationally was strongly hindered by the lack of an effective 3D numerical computational method. A persistent challenge is the fully-resolved time and history-dependent nature involved and the complicated elastodynamic solution itself. This work presents the first three dimensional discrete dislocation elastodynamics (DDE) method based on the fully-resolved elastodynamic framework.

The explicit formulas of the elastodynamic stress and strain fields of 3D non-uniformly moving dislocation loops are derived here. Several technical challenges are carefully examined and discussed. These include the method of effectively recording dislocation motion history, calculation of the velocity of a line source, calculation of retarded dislocation configurations, and treatment of space-time singularities, etc. Several benchmark cases are presented to carefully verify the method and to understand the features of the elastodynamic stress field. Excellent agreement with independent two dimensional calculations is shown. Then, for the first time, we present the stress field of a 3D moving shear dislocation loop. The difference between an expanding and a contracting loop, as well as the extent of the wave front singularity are discussed. As an application, we present how such elastodynamic effects remarkably influence the PK-force magnitude and sign on neighboring dislocations. This finding already implies expected remarkable effects of elastodynamics on most short-range dislocation interactions; a subject left for future investigations.

This work leads to plenty of room to further understand the fundamental mechanisms and physics of dislocations under shock loading conditions. For example, this investigation demonstrates that at finite time, retarded dislocations correspond to wave propagation between different straight dislocation positions. In the elastodynamics space, what the field point sees is generally a curved retarded dislocation, even for a straight dislocation (see Fig. 7). In other words, the apparent shape of a straight dislocation to a material observer is a curved one, perhaps viewed as space deformation induced by the high speed of motion! Therefore, the self force along a straight dislocation is no longer zero if elastodynamic effects are taken into account (Ni and Markenscoff, 2008; Pellegrini, 2012, 2014), except for the "radiation-free" straight segments moving at constant velocity for an infinitely long time (Weertman, 1969). At finite time, the self-force of a straight dislocation with constant velocity does not vanish (Pellegrini, 2014). This phenomenon cannot by captured, if one only considers the well-known inertia effect associated with the acceleration process in ad-hoc DDD simulations. In the current framework, such self-force and inertia effects are automatically captured. This will also avoid the artificiality of dealing with the effective mass of 3D mixed dislocations, since most of the existing effective mass equations are derived only for 2D edge or screw dislocations (Hirth et al., 1998; Ni and Markenscoff, 2008; Pellegrini, 2014). In addition, since elastodynamic effects are shown to have strong influence on short-range interactions, the basic evolution process of high-speed dislocations is expected to go beyond textbook descriptions of conventional dislocation behavior. It will be interesting to check the elastodynamic effects on the basic operation process of Frank-Read sources, junction formation, cross-slip, etc. Forthcoming investigations will be dedicated to disclose such intriguing phenomena, based on further efforts on the development of an effective mobility law of dislocations (Eshelby, 1953; Pellegrini, 2014; Pillon et al., 2007).

Acknowledgements

This material is based upon work supported by the National Science Foundation, Grant Numbers CMMI-1024353 and CMMI-1727740 at UCLA. Markus Lazar gratefully acknowledges a grant obtained from the Deutsche Forschungsgemeinschaft (grant number La1974/4-1). We wish to acknowledge the inspiring discussions with Professor Vijay Gupta and his group on their laser shock experiments, as well as the discussions with Prof. Artur R. Davoyan.

Appendix A. Derivation of Eq. (12) and Eq. (13)

The derivatives of the position vector **x** are introduced into Eq. (11) to obtain

$$\begin{aligned}G_{ij,k}(\mathbf{x},t) = \frac{-1}{4\pi\rho}\Bigg\{&\frac{1}{c_{\mathrm{T}}^{2}}\left(-\frac{\delta_{ij}x_k+\delta_{ik}x_j+\delta_{jk}x_i}{x^3}+\frac{3x_ix_jx_k}{x^5}\right)\delta\left(t-\frac{x}{c_{\mathrm{T}}}\right)+\frac{1}{c_{\mathrm{T}}^{2}r}\left(\delta_{ij}-\frac{x_ix_j}{x^2}\right)\left(\delta\left(t-\frac{x}{c_{\mathrm{T}}}\right)\right)_{,k}\\ &+\frac{1}{c_{\mathrm{L}}^{2}}\left(\frac{\delta_{ik}x_j+\delta_{jk}x_i}{x^3}-\frac{3x_ix_jx_k}{x^5}\right)\delta(t-\frac{x}{c_{\mathrm{L}}})+\frac{1}{c_{\mathrm{L}}^{2}}\frac{x_ix_j}{x^3}\left(\delta(t-\frac{x}{c_{\mathrm{L}}})\right)_{,k}\\ &+\left(\frac{3\delta_{ij}x_k+3\delta_{jk}x_i+3\delta_{ik}x_j}{x^5}-\frac{15x_ix_jx_k}{x^7}\right)\int_{x/c_{\mathrm{L}}}^{x/c_{\mathrm{T}}}\tau\delta\left(t-\tau\right)\mathrm{d}\tau+\left(\frac{3x_ix_j}{x^2}-\delta_{ij}\right)\frac{1}{x^3}\left(\int_{x/c_{\mathrm{L}}}^{x/c_{\mathrm{T}}}\tau\delta\left(t-\tau\right)\mathrm{d}\tau\right)_{,k}\Bigg\}.\end{aligned} \tag{A.1}$$

In Eq. (A.1), the following relations are met (Pujol, 2003):

$$\left(\delta(t-\frac{x}{c})\right)_{,k}=\frac{\partial\left(\delta(t-\frac{x}{c})\right)}{\partial(t-\frac{x}{c})}\frac{\partial(t-\frac{x}{c})}{\partial x_k}=\frac{-x_k}{cx}\partial_t\left(\delta(t-\frac{x}{c})\right), \tag{A.2}$$

$$\begin{aligned}\int_{x/c_{\mathrm{L}}}^{x/c_{\mathrm{T}}}\tau\delta\left(t-\tau\right)\mathrm{d}\tau &= \int_{-\infty}^{+\infty}\tau\left(H(\tau-\frac{x}{c_{\mathrm{L}}})-H(\tau-\frac{x}{c_{\mathrm{T}}})\right)\delta\left(t-\tau\right)\mathrm{d}\tau\\ &=\left(tH(t-\frac{x}{c_{\mathrm{L}}})-tH(t-\frac{x}{c_{\mathrm{T}}})\right)*\delta(t)=tH(t-\frac{x}{c_{\mathrm{L}}})-tH(t-\frac{x}{c_{\mathrm{T}}}),\end{aligned} \tag{A.3}$$

$$\begin{aligned}\left(\int_{x/c_{\mathrm{L}}}^{x/c_{\mathrm{T}}}\tau\delta\left(t-\tau\right)\mathrm{d}\tau\right)_{,k} &= \left(tH(t-\frac{x}{c_{\mathrm{L}}})-tH(t-\frac{x}{c_{\mathrm{T}}})\right)_{,k}=t\delta\left(t-\frac{x}{c_{\mathrm{L}}}\right)\left(-\frac{x_k}{rc_{\mathrm{L}}}\right)-t\delta\left(t-\frac{x}{c_{\mathrm{T}}}\right)\left(-\frac{x_k}{rc_{\mathrm{T}}}\right)\\ &=\frac{-x_k}{c_L^2}\delta\left(t-\frac{x}{c_{\mathrm{L}}}\right)+\frac{x_k}{c_T^2}\delta\left(t-\frac{x}{c_{\mathrm{T}}}\right).\end{aligned} \tag{A.4}$$

where $H(x)$ represents Heaviside step function, which is 1 when $x \geq 0$, and is 0 when $x < 0$.

Substituting Eq. (A.2) and Eq. (A.4) into Eq. (A.1), we obtain Eq. (12).

Similarly, we can calculate the time derivative of Green functions

$$\dot{G}_{ij}(\mathbf{x},t)=\frac{-1}{4\pi\rho x}\left\{\frac{1}{c_{\mathrm{T}}^{2}}\left(\delta_{ij}-\frac{x_ix_j}{x^2}\right)\partial_t\left(\delta\left(t-\frac{x}{c_{\mathrm{T}}}\right)\right)+\frac{1}{c_{\mathrm{L}}^{2}}\frac{x_ix_j}{x^2}\partial_t\left(\delta\left(t-\frac{x}{c_{\mathrm{L}}}\right)\right)+\left(\frac{3x_ix_j}{x^2}-\delta_{ij}\right)\frac{1}{x^2}\partial_t\left(\int_{x/c_{\mathrm{L}}}^{x/c_{\mathrm{T}}}\tau\delta\left(t-\tau\right)\mathrm{d}\tau\right)\right\}, \tag{A.5}$$

where according to Eq. (A.3),

$$\begin{aligned}\partial_t\left(\int_{x/c_{\mathrm{L}}}^{x/c_{\mathrm{T}}}\tau\delta\left(t-\tau\right)\mathrm{d}\tau\right) &= H(t-\frac{x}{c_{\mathrm{L}}})-H(t-\frac{x}{c_{\mathrm{T}}})+\frac{x}{c_{\mathrm{L}}}\delta\left(t-\frac{x}{c_{\mathrm{L}}}\right)-\frac{x}{c_{\mathrm{T}}}\delta\left(t-\frac{x}{c_{\mathrm{T}}}\right)\\ &=\int_{x/c_{\mathrm{L}}}^{x/c_{\mathrm{T}}}\delta\left(t-\tau\right)\mathrm{d}\tau+\frac{x}{c_{\mathrm{L}}}\delta\left(t-\frac{x}{c_{\mathrm{L}}}\right)-\frac{x}{c_{\mathrm{T}}}\delta\left(t-\frac{x}{c_{\mathrm{T}}}\right).\end{aligned} \tag{A.6}$$

Appendix B. Stress field regularization process

This appendix aims to give a derivation of equations to remove the dislocation core singularity by extending Cai et al.'s static regularization method (Cai et al., 2006) to 3D elastodynamics case. Note that this is just an approximate treatment to remove the spatial singularity. Further work is required to develop a strict mathematical derivation through convolution of the Green tensor by a regularization function. Using derivatives of the radius vector, we have

$$
\begin{aligned}
\frac{R_i}{R^3} &= -\frac{R_{,imm}}{2}, \\
\frac{R_iR_jR_k}{R^5} &= \frac{1}{3}\left(R_{,ijk} + \frac{R_i\delta_{jk} + R_j\delta_{ik} + R_k\delta_{ij}}{R^3}\right) = \frac{1}{3}\left(R_{,ijk} - \frac{R_{,imm}\delta_{jk} + R_{,jmm}\delta_{ik} + R_{,kmm}\delta_{ij}}{2}\right), \\
\frac{1}{R} &= \frac{R_{,mm}}{2}, \\
\frac{R_iR_j}{R^3} &= \frac{R_{,mm}\delta_{ij}}{2} - R_{,ij}.
\end{aligned}
\tag{B.1}
$$

When one replaces displacement vector R by $R_a = \sqrt{R^2 + a^2}$, where a is the dislocation core size, the following relations are obtained:

$$
\begin{aligned}
R_{a,i} &= \frac{R_i}{R_a}, \\
R_{a,ip} &= \frac{\delta_{ip}}{R_a} - \frac{R_iR_p}{R_a^3}, \\
R_{a,pp} &= \frac{2}{R_a} + \frac{a^2}{R_a^3}, \\
R_{a,ipp} &= \frac{-2R_i}{R_a^3} - \frac{3R_ia^2}{R_a^5}, \\
R_{a,ijk} &= \frac{3R_iR_jR_K}{R_a^5} - \frac{R_i\delta_{jk} + R_j\delta_{ik} + R_k\delta_{ij}}{R_a^3}.
\end{aligned}
\tag{B.2}
$$

The relations above suggest that one cannot just replace $1/R^n$ by $1/R_a^n$, because the Laplace operator will induce additional a^2 terms. Therefore, Eq. (B.1) should be replaced by

$$
\begin{aligned}
\frac{R_i}{R^3} &\rightarrow -\frac{R_{a,imm}}{2} = \left(1 + \frac{3a^2}{2R_a^2}\right)\frac{R_i}{R_a^3}, \\
\frac{R_iR_jR_k}{R^5} &\rightarrow \frac{1}{3}\left(R_{a,ijk} - \frac{R_{a,imm}\delta_{jk} + R_{a,jmm}\delta_{ik} + R_{a,kmm}\delta_{ij}}{2}\right) = \frac{R_iR_jR_k}{R_a^5} + \frac{a^2}{2R_a^5}\left(R_i\delta_{jk} + R_j\delta_{ik} + R_k\delta_{ij}\right), \\
\frac{1}{R} &\rightarrow \frac{R_{a,mm}}{2} = (1 + \frac{a^2}{2R_a^2})\frac{1}{R_a}, \\
\frac{R_iR_j}{R^3} &\rightarrow \frac{R_{a,mm}\delta_{ij}}{2} - R_{a,ij} = \frac{R_iR_j}{R_a^3} + \frac{a^2\delta_{ij}}{2R_a^3}.
\end{aligned}
\tag{B.3}
$$

Accordingly, in Eq. (22), the key terms are replaced by

$$\begin{aligned}
\frac{\mathbf{R}\otimes(\mathbf{b}\times\boldsymbol{\xi})}{R^3} &\to \left(1+\frac{3a^2}{2R_a^2}\right)\frac{\mathbf{R}\otimes(\mathbf{b}\times\boldsymbol{\xi})}{R_a^3},\\
\frac{\mathbf{b}\cdot(\mathbf{R}\times\boldsymbol{\xi})\mathbf{I}}{R^3} &\to \left(1+\frac{3a^2}{2R_a^2}\right)\frac{\mathbf{b}\cdot(\mathbf{R}\times\boldsymbol{\xi})\mathbf{I}}{R_a^3},\\
\frac{\mathbf{b}\otimes(\mathbf{R}\times\boldsymbol{\xi})}{R^3} &\to \left(1+\frac{3a^2}{2R_a^2}\right)\frac{\mathbf{b}\otimes(\mathbf{R}\times\boldsymbol{\xi})}{R_a^3},\\
\frac{(\mathbf{R}\cdot\mathbf{b})\mathbf{R}\otimes(\mathbf{R}\times\boldsymbol{\xi})}{R^5} &\to \frac{(\mathbf{R}\cdot\mathbf{b})\mathbf{R}\otimes(\mathbf{R}\times\boldsymbol{\xi})}{R_a^5}+\frac{a^2}{2R_a^5}\left(\mathbf{R}\otimes(\mathbf{b}\times\boldsymbol{\xi})+\mathbf{b}\otimes(\mathbf{R}\times\boldsymbol{\xi})\right),\\
\frac{\mathbf{b}\cdot(\mathbf{V}\times\boldsymbol{\xi})\mathbf{I}}{R} &\to \left(1+\frac{a^2}{2R_a^2}\right)\frac{\mathbf{b}\cdot(\mathbf{V}\times\boldsymbol{\xi})\mathbf{I}}{R_a},\\
\frac{(\mathbf{R}\cdot\mathbf{b})\mathbf{R}\cdot(\mathbf{V}\times\boldsymbol{\xi})\mathbf{I}}{R^3} &\to \frac{(\mathbf{R}\cdot\mathbf{b})\mathbf{R}\cdot(\mathbf{V}\times\boldsymbol{\xi})\mathbf{I}}{R_a^3}+\frac{a^2}{2R_a^3}\mathbf{b}\cdot(\mathbf{V}\times\boldsymbol{\xi})\mathbf{I},\\
\frac{\mathbf{b}\otimes(\mathbf{V}\times\boldsymbol{\xi})}{R} &\to \left(1+\frac{a^2}{2R_a^2}\right)\frac{\mathbf{b}\otimes(\mathbf{V}\times\boldsymbol{\xi})}{R_a},\\
\frac{(\mathbf{R}\cdot\mathbf{b})\mathbf{R}\otimes(\mathbf{V}\times\boldsymbol{\xi})}{R^3} &\to \frac{(\mathbf{R}\cdot\mathbf{b})\mathbf{R}\otimes(\mathbf{V}\times\boldsymbol{\xi})}{R_a^3}+\frac{a^2}{2R_a^3}\mathbf{b}\otimes(\mathbf{V}\times\boldsymbol{\xi}).
\end{aligned}\tag{B.4}$$

Note that for the fourth equation in Eq. (B.4), one antisymmetric term is ignored because it does not contributes to the symmetry stress σ. By substituting Eq. (B.4) into Eq. (22), we obtain

$$
\begin{aligned}
\mathbf{s}(\mathbf{x},t) = \oint_{\mathcal{L}(t-R/c_\mathrm{T})} & \frac{1}{R_a^2\,(R_a-\mathbf{R}\cdot\mathbf{V}/c_\mathrm{T})}\Bigg(\bigg(-2+\frac{3a^2}{R_a^2}\bigg)\mathbf{R}\otimes(\mathbf{b}\times\boldsymbol{\xi})+\frac{-\nu}{1-2\nu}\bigg(1+\frac{3a^2}{2R_a^2}\bigg)\mathbf{b}\cdot(\mathbf{R}\times\boldsymbol{\xi})\mathbf{I}\\
&-3\Bigg(\bigg(1-\frac{a^2}{2R_a^2}\bigg)\mathbf{b}-4\frac{\mathbf{R}\cdot\mathbf{b}}{R_a^2}\mathbf{R}\Bigg)\otimes(\mathbf{R}\times\boldsymbol{\xi})\Bigg)\mathrm{d}L'\\
-\partial_t\oint_{\mathcal{L}(t-R/c_\mathrm{T})} & \frac{1}{c_\mathrm{T}R_a\,(R_a-\mathbf{R}\cdot\mathbf{V}/c_\mathrm{T})}\Bigg(\frac{-a^2}{R_a^2}\mathbf{R}\otimes(\mathbf{b}\times\boldsymbol{\xi})+\bigg(1+\frac{3a^2}{2R_a^2}\bigg)\frac{\nu}{1-2\nu}\mathbf{b}\cdot(\mathbf{R}\times\boldsymbol{\xi})\mathbf{I}\\
&+\Bigg(\bigg(1+\frac{a^2}{2R_a^2}\bigg)\mathbf{b}-\frac{2\mathbf{R}\cdot\mathbf{b}}{R_a^2}\mathbf{R}\Bigg)\otimes(\mathbf{R}\times\boldsymbol{\xi})\Bigg)\mathrm{d}L'\\
+\oint_{\mathcal{L}(t-R/c_\mathrm{L})} & \frac{1-2\nu}{(1-\nu)R_a^2\,(R_a-\mathbf{R}\cdot\mathbf{V}/c_\mathrm{L})}\Bigg(\bigg(\frac{1-3\nu}{1-2\nu}+\frac{-3+3\nu}{2(1-2\nu)}\frac{a^2}{R_a^2}\bigg)\mathbf{R}\otimes(\mathbf{b}\times\boldsymbol{\xi})\\
&+\frac{\nu^2}{(1-2\nu)^2}\bigg(1+\frac{3a^2}{2R_a^2}\bigg)\mathbf{b}\cdot(\mathbf{R}\times\boldsymbol{\xi})\mathbf{I}+\Bigg(\bigg(1-\frac{3a^2}{2R_a^2}\bigg)\mathbf{b}-\frac{6\mathbf{R}\cdot\mathbf{b}}{R^2}\mathbf{R}\Bigg)\otimes(\mathbf{R}\times\boldsymbol{\xi})\Bigg)\mathrm{d}L'\\
-\partial_t\oint_{\mathcal{L}(t-R/c_\mathrm{L})} & \frac{1-2\nu}{(1-\nu)c_\mathrm{L}R_a\,(R_a-\mathbf{R}\cdot\mathbf{V}/c_\mathrm{L})}\Bigg(\bigg(\frac{\nu}{1-2\nu}+\frac{1+\nu}{2(1-2\nu)}\frac{a^2}{R_a^2}\bigg)\mathbf{R}\otimes(\mathbf{b}\times\boldsymbol{\xi})\\
&-\bigg(1+\frac{3a^2}{2R_a^2}\bigg)\frac{\nu^2}{(1-2\nu)^2}\mathbf{b}\cdot(\mathbf{R}\times\boldsymbol{\xi})\mathbf{I}+\bigg(\frac{a^2}{2R_a^2}\mathbf{b}+\frac{\mathbf{R}\cdot\mathbf{b}}{R^2}\mathbf{R}\bigg)\otimes(\mathbf{R}\times\boldsymbol{\xi})\Bigg)\mathrm{d}L'\\
+\int_{1/c_\mathrm{L}}^{1/c_\mathrm{T}}\oint_{\mathcal{L}(t-R\kappa)} & \frac{6c_\mathrm{T}^2\kappa}{R_a^2\,(R_a-\mathbf{R}\cdot\mathbf{V}\kappa)}\Bigg(\bigg(1-\frac{a^2}{R_a^2}\bigg)\mathbf{R}\otimes(\mathbf{b}\times\boldsymbol{\xi})+\Bigg(\bigg(1-\frac{a^2}{R_a^2}\bigg)\mathbf{b}-\frac{5\mathbf{R}\cdot\mathbf{b}}{R^2}\mathbf{R}\Bigg)\otimes(\mathbf{R}\times\boldsymbol{\xi})\Bigg)\mathrm{d}L'\mathrm{d}\kappa\\
+\partial_t\oint_{\mathcal{L}(t-R/c_\mathrm{T})} & \frac{1}{c_\mathrm{T}^2\,(R_a-\mathbf{R_a}\cdot\mathbf{V}/c_\mathrm{T})}\Bigg(\frac{\nu}{1-2\nu}\bigg(\mathbf{b}-\frac{\mathbf{R}\cdot\mathbf{b}}{R_a^2}\mathbf{R}\bigg)\cdot(\mathbf{V}\times\boldsymbol{\xi})\mathbf{I}+\bigg(\mathbf{b}-\frac{\mathbf{R}\cdot\mathbf{b}}{R_a^2}\mathbf{R}\bigg)\otimes(\mathbf{V}\times\boldsymbol{\xi})\Bigg)\mathrm{d}L'\\
+\partial_t\oint_{\mathcal{L}(t-R/c_\mathrm{L})} & \frac{1}{c_\mathrm{L}^2\,(R_a-\mathbf{R}\cdot\mathbf{V}/c_\mathrm{L})}\Bigg(\frac{\nu}{1-2\nu}\bigg(\frac{a^2}{2R_a^2}\mathbf{b}+\frac{\mathbf{R}\cdot\mathbf{b}}{R_a^2}\mathbf{R}\bigg)\cdot(\mathbf{V}\times\boldsymbol{\xi})\mathbf{I}+\bigg(\frac{a^2}{2R_a^2}\mathbf{b}+\frac{\mathbf{R}\cdot\mathbf{b}}{R_a^2}\mathbf{R}\bigg)\otimes(\mathbf{V}\times\boldsymbol{\xi})\Bigg)\mathrm{d}L'\\
-\int_{1/c_\mathrm{L}}^{1/c_\mathrm{T}}\oint_{\mathcal{L}(t-R\kappa)} & \frac{1}{R_a\,(R_a-\mathbf{R}\cdot\mathbf{V}\kappa)}\Bigg(\frac{\nu}{1-2\nu}\Bigg(\bigg(1-\frac{a^2}{R_a^2}\bigg)\mathbf{b}-\frac{3\mathbf{R}\cdot\mathbf{b}}{R_a^2}\mathbf{R}\Bigg)\cdot(\mathbf{V}\times\boldsymbol{\xi})\mathbf{I}+\Bigg(\bigg(1-\frac{a^2}{R_a^2}\bigg)\mathbf{b}-\frac{3\mathbf{R}\cdot\mathbf{b}}{R_a^2}\mathbf{R}\Bigg)\otimes(\mathbf{V}\times\boldsymbol{\xi})\Bigg)\mathrm{d}L'\mathrm{d}\kappa\\
+\oint_{\mathcal{L}(t-R/c_\mathrm{T})} & \frac{1}{c_\mathrm{T}R_a\,(R_a-\mathbf{R}\cdot\mathbf{V}/c_\mathrm{T})}\Bigg(\frac{\nu}{1-2\nu}\Bigg(\bigg(1-\frac{a^2}{R_a^2}\bigg)\mathbf{b}-\frac{3\mathbf{R}\cdot\mathbf{b}}{R_a^2}\mathbf{R}\Bigg)\cdot(\mathbf{V}\times\boldsymbol{\xi})\mathbf{I}+\Bigg(\bigg(1-\frac{a^2}{R_a^2}\bigg)\mathbf{b}-\frac{3\mathbf{R}\cdot\mathbf{b}}{R_a^2}\mathbf{R}\Bigg)\otimes(\mathbf{V}\times\boldsymbol{\xi})\Bigg)\mathrm{d}L'\\
-\oint_{\mathcal{L}(t-R/c_\mathrm{L})} & \frac{1}{c_\mathrm{L}R_a\,(R_a-\mathbf{R}\cdot\mathbf{V}/c_\mathrm{L})}\Bigg(\frac{\nu}{1-2\nu}\Bigg(\bigg(1-\frac{a^2}{R_a^2}\bigg)\mathbf{b}-\frac{3\mathbf{R}\cdot\mathbf{b}}{R_a^2}\mathbf{R}\Bigg)\cdot(\mathbf{V}\times\boldsymbol{\xi})\mathbf{I}+\Bigg(\bigg(1-\frac{a^2}{R_a^2}\bigg)\mathbf{b}-\frac{3\mathbf{R}\cdot\mathbf{b}}{R_a^2}\mathbf{R}\Bigg)\otimes(\mathbf{V}\times\boldsymbol{\xi})\Bigg)\mathrm{d}L'.
\end{aligned}
\tag{B.5}
$$

Appendix C. Derivation of Eq. (32) and Eq. (33)

In order to obtain Eq. (32) and Eq. (33), we used Eq. (31) and the following relations:

$$
\begin{aligned}
\partial_t\oint_{\mathcal{L}(t-R/c_\mathrm{T})}\frac{x_3}{R\,(R-\mathbf{R}\cdot\mathbf{V}/c_\mathrm{T})}\mathrm{d}L' &= \partial_t\int_{-\sqrt{c_\mathrm{T}^2t^2-l^2}}^{\sqrt{c_\mathrm{T}^2t^2-l^2}}\frac{x_3}{R^2}\mathrm{d}x_3=\partial_t\left(ln(l^2+x_3^2)|_{-\sqrt{c_\mathrm{T}^2t^2-l^2}}^{\sqrt{c_\mathrm{T}^2t^2-l^2}}\right)=0,\\
\partial_t\oint_{\mathcal{L}(t-R/c_\mathrm{T})}\frac{1}{R^3\,(R-\mathbf{R}\cdot\mathbf{V}/c_\mathrm{T})}\mathrm{d}L' &= \partial_t\int_{-\sqrt{c_\mathrm{T}^2t^2-l^2}}^{\sqrt{c_\mathrm{T}^2t^2-l^2}}\frac{1}{R^4}\mathrm{d}x_3=\frac{2}{c_\mathrm{T}^2t^3\sqrt{c_\mathrm{T}^2t^2-l^2}}\mathrm{H}(c_\mathrm{T}t-l),\\
\partial_t\oint_{\mathcal{L}(t-R/c_\mathrm{T})}\frac{x_3}{R^3\,(R-\mathbf{R}\cdot\mathbf{V}/c_\mathrm{T})}\mathrm{d}L' &= \partial_t\int_{-\sqrt{c_\mathrm{T}^2t^2-l^2}}^{\sqrt{c_\mathrm{T}^2t^2-l^2}}\frac{x_3}{R^4}\mathrm{d}x_3=\partial_t\left(-\frac{1}{2(l^2+x_3^2)}|_{-\sqrt{c_\mathrm{T}^2t^2-l^2}}^{\sqrt{c_\mathrm{T}^2t^2-l^2}}\right)=0,
\end{aligned}
\tag{C.1}
$$

$$\begin{aligned}
\mathbf{b}\cdot(\mathbf{R}\times\boldsymbol{\xi})\mathbf{I} &= bR_2(\mathbf{e}_1\mathbf{e}_1+\mathbf{e}_2\mathbf{e}_2+\mathbf{e}_3\mathbf{e}_3),\\
(\mathbf{R}\times\boldsymbol{\xi})\otimes\mathbf{b}+\mathbf{b}\otimes(\mathbf{R}\times\boldsymbol{\xi}) &= 2bR_2\mathbf{e}_1\mathbf{e}_1-bR_1(\mathbf{e}_1\mathbf{e}_2+\mathbf{e}_2\mathbf{e}_1),\\
(\mathbf{R}\cdot\mathbf{b})(\mathbf{R}\otimes(\mathbf{R}\times\boldsymbol{\xi})+(\mathbf{R}\times\boldsymbol{\xi})\otimes\mathbf{R}) &= bR_1\Big(2R_1R_2(\mathbf{e}_1\mathbf{e}_1-\mathbf{e}_2\mathbf{e}_2)+(R_2^2-R_1^2)(\mathbf{e}_1\mathbf{e}_2+\mathbf{e}_2\mathbf{e}_1)\\
&\quad +R_3R_2(\mathbf{e}_1\mathbf{e}_3+\mathbf{e}_3\mathbf{e}_1)-R_1R_3(\mathbf{e}_2\mathbf{e}_3+\mathbf{e}_3\mathbf{e}_2)\Big),\\
\mathbf{R}\otimes(\mathbf{b}\times\boldsymbol{\xi})+(\mathbf{b}\times\boldsymbol{\xi})\otimes\mathbf{R} &= -2bR_2\mathbf{e}_2\mathbf{e}_2-bR_1(\mathbf{e}_1\mathbf{e}_2+\mathbf{e}_2\mathbf{e}_1)-bR_3(\mathbf{e}_2\mathbf{e}_3+\mathbf{e}_3\mathbf{e}_2).
\end{aligned} \tag{C.2}$$

Appendix D. More validation test results

Fig. D1 shows very good agreement between 3D and 2D calculations for different stress components at the same time, for an injected static edge dislocation.

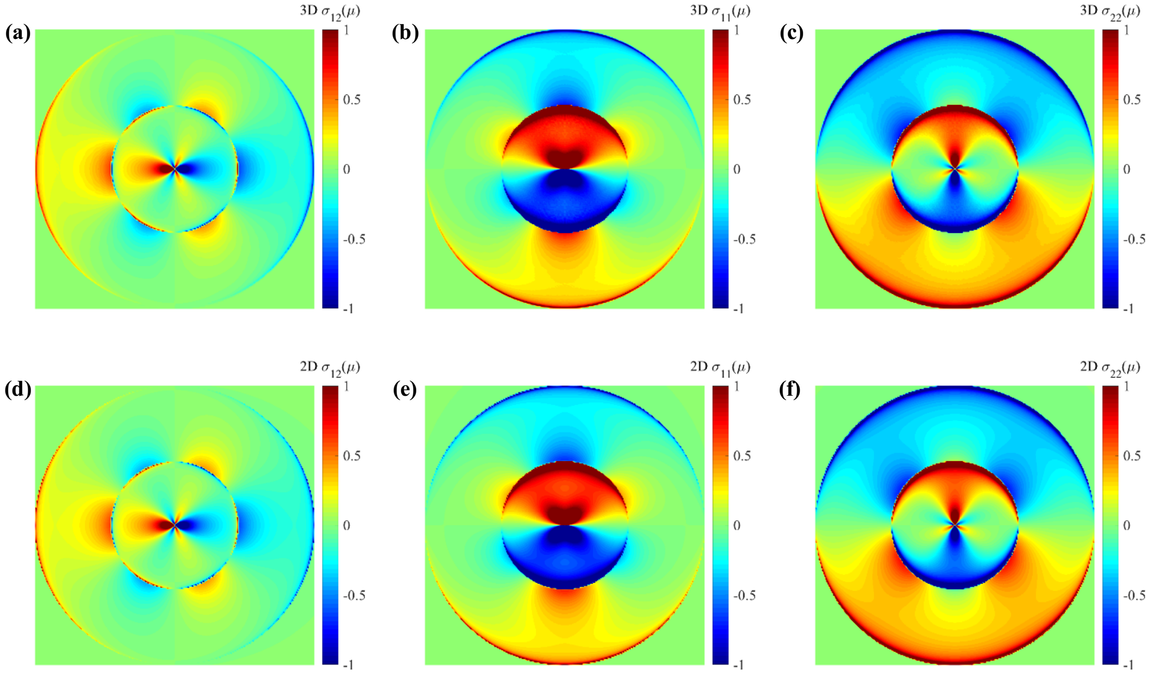

Figure D1: Different stress components σ_{12}, σ_{11}, σ_{22} of an injected static edge dislocations on plane GHIJ in Fig. 6 (a) (unit: μ), here $L_1 = L_2 = 2.5b$, $t = 1.136b/c_T$. (a-c) are obtained by our 3D DDE, (d-f) are obtained by 2D solution

Fig. D2 gives the stress field of a uniformly moving dislocation with velocity $0.8c_T$ from static rest conditions (i.e. the dislocation existed at initial time and not injected as in the previous case). Good consistency with the 2D solution is also observed, including the stress distribution along x_2=0.147b, as shown in Fig. D2(c). One notices that the stress field at the wave front for an initially static dislocation is much weaker than that for a suddenly injected dislocation (compare Fig. D2 to Fig. 10). This also demonstrates the strong history dependence of the dislocation stress field.

Achenbach, J. D. (2003). *Reciprocity in elastodynamics*. Cambridge University Press.

Anderson, J. L. (1992). Why we use retarded potentials. *American journal of physics 60*(5), 465–467.

Bringa, E., K. Rosolankova, R. Rudd, B. Remington, J. Wark, M. Duchaineau, D. Kalantar, J. Hawreliak, and J. Belak (2006). Shock deformation of face-centred-cubic metals on subnanosecond timescales. *Nature materials 5*(10), 805.

Bringa, E. M., A. Caro, Y. Wang, M. Victoria, J. M. McNaney, B. A. Remington, R. F. Smith, B. R. Torralva, and H. Van Swygenhoven (2005). Ultrahigh strength in nanocrystalline materials under shock loading. *Science 309*(5742), 1838–1841.

Cai, W., A. Arsenlis, C. R. Weinberger, and V. V. Bulatov (2006). A non-singular continuum theory of dislocations. *Journal of the Mechanics and Physics of Solids 54*(3), 561–587.

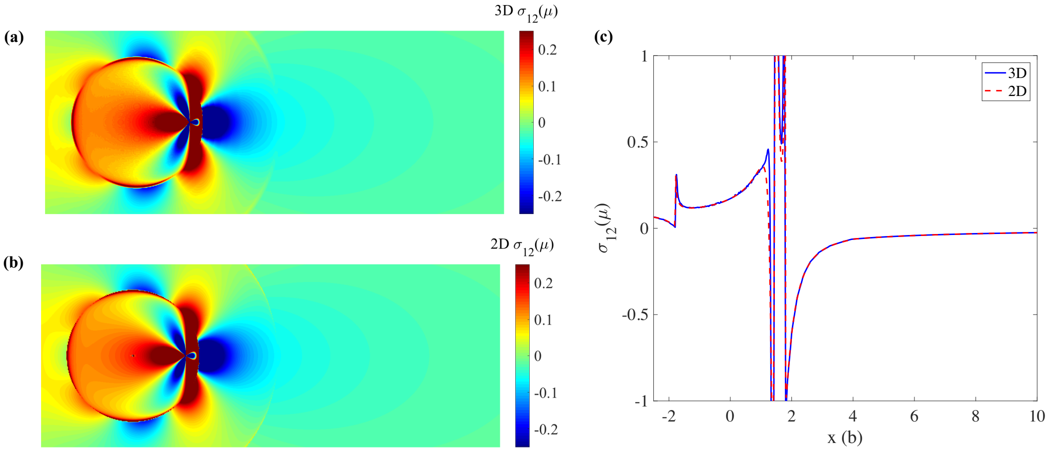

Figure D2: σ_{12} of a preexisting edge dislocation moving at a uniform velocity $V = 0.8c_T$ on the plane GHIJ in Fig. 6 (a), here $L_1 = 12.5b$, $L_2 = 5b$, $t = 1.8b/c_T$. (a) 3D DDE simulation results (b) 2D results. (c) Stress distribution along x_2=0.147b.

Callias, C. and X. Markenscoff (1988). Singular asymptotics of integrals and the near-field radiated from nonuniformly moving dislocations. *Archive for Rational Mechanics and Analysis 102*(3), 273–285.

Callias, C., X. Markenscoff, and L. Q. Ni (1990). A singular asymptotic expansion for the field near a moving dislocation loop. *Quarterly of applied mathematics 48*(1), 113–132.

Cao, B. Y., D. H. Lassila, M. S. Schneider, B. K. Kad, C. X. Huang, Y. B. Xu, D. H. Kalantar, B. A. Remington, and M. A. Meyers (2005). Effect of shock compression method on the defect substructure in monocrystalline copper. *Materials Science and Engineering: A 409*(1-2), 270–281.

Carley, M. (2003). Retarded-time calculation for moving sources. *AIAA journal 41*(5), 967–969.

Casalino, D. (2003). An advanced time approach for acoustic analogy predictions. *Journal of Sound and Vibration 261*(4), 583–612.

Chu, H., J. Wang, and I. Beyerlein (2012). Anomalous reactions of a supersonic coplanar dislocation dipole: Bypass or twinning? *Scripta Materialia 67*(1), 69–72.

Clifton, R. and X. Markenscoff (1981). Elastic precursor decay and radiation from nonuniformly moving dislocations. *Journal of the Mechanics and Physics of Solids 29*(3), 227 – 251.

Colorado, H., A. Navarro, S. Prikhodko, J. Yang, N. Ghoniem, and V. Gupta (2013). Ultrahigh strain-rate bending of copper nanopillars with laser-generated shock waves. *Journal of Applied Physics 114*(23), 233510.

Cui, Y., G. Po, and N. M. Ghoniem (2018). A coupled dislocation dynamics-continuum barrier field model with application to irradiated materials. *International Journal of Plasticity 104*, 54–67.

de Wit', R. (1960). The continuum theory of stationary dislocations. *Solid State Physics 10*, 249–292.

Eringen, A. C., E. S. Suhubi, and D. R. Bland (1977). Elastodynamics, vols. 1 and 2. *Physics Today 30*, 65.

Eshelby, J. (1949). Uniformly moving dislocations. *Proceedings of the Physical Society. Section A 62*(5), 307.

Eshelby, J. (1953). The equation of motion of a dislocation. *Physical Review 90*(2), 248.

Eshelby, J. (1956). Supersonic dislocations and dislocations in dispersive media. *Proceedings of the Physical Society. Section B 69*(10), 1013.

Frank, F. (1949). On the equations of motion of crystal dislocations. *Proceedings of the Physical Society. Section A 62*(2), 131.

Ghoniem, N. M. and L. Sun (1999). Fast-sum method for the elastic field of three-dimensional dislocation ensembles. *Physical Review B 60*(1), 128.

Ghoniem, N., M, S.-H. Tong, and L. Sun (2000). Parametric dislocation dynamics: a thermodynamics-based approach to investigations of mesoscopic plastic deformation. *Physical Review B 61*(2), 913.

Gumbsch, P. and H. Gao (1999). Dislocations faster than the speed of sound. *Science 283*(5404), 965–968.

Gurrutxaga-Lerma, B., D. S. Balint, D. Dini, D. E. Eakins, and A. P. Sutton (2013). A dynamic discrete dislocation plasticity method for the simulation of plastic relaxation under shock loading. In *Proc. R. Soc. A*, Volume 469, pp. 20130141. The Royal Society.

Gurrutxaga-Lerma, B., D. S. Balint, D. Dini, D. E. Eakins, and A. P. Sutton (2015a). Attenuation of the dynamic yield point of shocked aluminum using elastodynamic simulations of dislocation dynamics. *Phys. Rev. Lett. 114*, 174301.

Gurrutxaga-Lerma, B., D. S. Balint, D. Dini, and A. P. Sutton (2015b). Elastodynamic image forces on dislocations. In *Proc. R. Soc. A*, Volume 471, pp. 20150433. The Royal Society.

Hirth, J. P. and J. Lothe (1982). *Theory of dislocations*. John Wiley & Sons.

Hirth, J., H. Zbib, and J. Lothe (1998). Forces on high velocity dislocations. *Modelling and Simulation in Materials Science and Engineering 6*(2), 165.

Hu, J., Z. Liu, K. Chen, and Z. Zhuang (2017). Investigations of shock-induced deformation and dislocation mechanism by a multiscale discrete dislocation plasticity model. *Computational Materials Science 131*, 78–85.

Jackson, J. D. (2012). *Classical electrodynamics*. John Wiley & Sons.

Jiang, S., Z. Chen, Y. Gan, S. Y. Oloriegbe, T. D. Sewell, and D. L. Thompson (2012). Size effects on the wave propagation and deformation pattern in copper nanobars under symmetric longitudinal impact loading. *Journal of Physics D: Applied Physics 45*(47), 475305.

Landau, L. D. and E. M. Lifshitz (1971). The classical theory of fields.

Lazar, M. (2009). The gauge theory of dislocations: a uniformly moving screw dislocation. In *Proceedings of the Royal Society of London A: Mathematical, Physical and Engineering Sciences*, Volume 465, pp. 2505–2520. The Royal Society.

Lazar, M. (2013a). The fundamentals of non-singular dislocations in the theory of gradient elasticity: Dislocation loops and straight dislocations. *International Journal of Solids and Structures 50*(2), 352–362.

Lazar, M. (2013b). On the non-uniform motion of dislocations: the retarded elastic fields, the retarded dislocation tensor potentials and the liénard–wiechert tensor potentials. *Philosophical Magazine 93*(7), 749–776.

Lazar, M. (2014). On gradient field theories: gradient magnetostatics and gradient elasticity. *Philosophical Magazine 94*(25), 2840–2874.

Lazar, M. and Y.-P. Pellegrini (2016). Distributional and regularized radiation fields of non-uniformly moving straight dislocations, and elastodynamic tamm problem. *Journal of the Mechanics and Physics of Solids 96*, 632–659.

Li, Q.-J., J. Li, Z.-W. Shan, and E. Ma (2016). Strongly correlated breeding of high-speed dislocations. *Acta Materialia 119*, 229–241.

Liu, Z., X. You, and Z. Zhuang (2008). A mesoscale investigation of strain rate effect on dynamic deformation of single-crystal copper. *International Journal of Solids and Structures 45*(13), 3674–3687.

Longère, P. and A. Dragon (2015). Dynamic vs. quasi-static shear failure of high strength metallic alloys: Experimental issues. *Mechanics of Materials 80*, 203–218.

Lu, L., R. Schwaiger, Z. Shan, M. Dao, K. Lu, and S. Suresh (2005). Nano-sized twins induce high rate sensitivity of flow stress in pure copper. *Acta materialia 53*(7), 2169–2179.

Luscher, D. J., F. L. Addessio, M. J. Cawkwell, and K. J. Ramos (2017). A dislocation density-based continuum model of the anisotropic shock response of single crystal α-cyclotrimethylene trinitramine. *Journal of the Mechanics and Physics of Solids 98*, 63–86.

Markenscoff, X. and R. Clifton (1981). The nonuniformly moving edge dislocation. *Journal of the Mechanics and Physics of Solids 29*(3), 253–262.

Markenscoff, X. (1983). On the dislocation fields in terms of the dynamic green's function. *Journal of elasticity 13*(3), 237–241.

Markenscoff, X. and L. Ni (1990). The singular nature of the stress field near an arbitrarily moving dislocation loop. *Journal of the Mechanics and Physics of Solids 38*(4), 481–490.

Markenscoff, X. (2010). Evolution equation of moving defects: dislocations and inclusions. *International journal of fracture 166*(1-2), 35–40.

Meyers, M. A. (1994). *Dynamic behavior of materials*. John Wiley & Sons.

Mura, T. (1963). Continuous distribution of moving dislocations. *Philosophical Magazine 8*(89), 843–857.

Ni, L. and X. Markenscoff (2008). The self-force and effective mass of a generally accelerating dislocation i: Screw dislocation. *Journal of the Mechanics and Physics of Solids 56*(4), 1348–1379.

Ni, L. and X. Markenscoff (2016). The self-similarly expanding eshelby ellipsoidal inclusion: I. field solution. *Journal of the Mechanics and Physics of Solids 96*, 683–695.

Nosenko, V., S. Zhdanov, and G. Morfill (2007). Supersonic dislocations observed in a plasma crystal. *Physical review letters 99*(2), 025002.

Pang, B., S. Case, I. Jones, J. Millett, G. Whiteman, Y. Chiu, and C. Bronkhorst (2018). The defect evolution in shock loaded tantalum single crystals. *Acta Materialia 148*, 482–491.

Pellegrini, Y.-P. (2012). Screw and edge dislocations with time-dependent core width: from dynamical core equations to an equation of motion. *Journal of the Mechanics and Physics of Solids 60*(2), 227–249.

Pellegrini, Y.-P. (2014). Equation of motion and subsonic-transonic transitions of rectilinear edge dislocations: A collective-variable approach. *Physical Review B 90*(5), 054120.

Pellegrini, Y.-P. and M. Lazar (2015). On the gradient of the green tensor in two-dimensional elastodynamic problems, and related integrals: Distributional approach and regularization, with application to nonuniformly moving sources. *Wave Motion 57*, 44–63.

Pillon, L. and C. Denoual (2009). Inertial and retardation effects for dislocation interactions. *Philosophical Magazine 89*(2), 127–141.

Pillon, L., C. Denoual, and Y.-P. Pellegrini (2007). Equation of motion for dislocations with inertial effects. *Physical Review B 76*(22), 224105.

Po, G. and N. Ghoniem (2014a). A variational formulation of constrained dislocation dynamics coupled with heat and vacancy diffusion. *Journal of the Mechanics and Physics of Solids 66*, 103–116.

Po, G., M. Lazar, D. Seif, and N. Ghoniem (2014b). Singularity-free dislocation dynamics with strain gradient elasticity. *Journal of the Mechanics and Physics of Solids 68*, 161–178.

Po, G., M. S. Mohamed, T. Crosby, C. Erel, A. El-Azab, and N. Ghoniem (2014c). Recent progress in discrete dislocation dynamics and its applications to micro plasticity. *JOM 66*(10), 2108–2120.

Po, G. and N. Ghoniem (2015). Mechanics of defect evolution library, model. ⟨*https://bitbucket.org/model/model/wiki/home*⟩.

Po, G., M. Lazar, N. C. Admal, and N. Ghoniem (2018). A non-singular theory of dislocations in anisotropic crystals. *International Journal of Plasticity 103*, 1–22.

Pujol, J. (2003). *Elastic wave propagation and generation in seismology*. Cambridge University Press.

Scovazzi, G. and T. Hughes (2007). Lecture notes on continuum mechanics on arbitrary moving domains. *Lecture Notes, November*.

Seif, D., G. Po, R. Crum, V. Gupta, and N. M. Ghoniem (2014). Shock-induced plasticity and the Hugoniot elastic limit in copper nano films and rods. *Journal of Applied Physics 115*(5), 054301.

Shehadeh, M. A., H. M. Zbib, and T. D. De la Rubia (2005). Multiscale dislocation dynamics simulations of shock compression in copper single crystal. *International journal of plasticity 21*(12), 2369–2390.

Shehadeh, M. A. and H. M. Zbib (2016). On the homogeneous nucleation and propagation of dislocations under shock compression. *Philosophical Magazine 96*(26), 2752–2778.

Stroh, A. N. (1962). Force on a moving dislocation. *Physical Review 128*(1), 55.

Wang, Z. and I. Beyerlein (2008). Stress orientation and relativistic effects on the separation of moving screw dislocations. *Physical Review B 77*(18), 184112.

Weertman, J. (1969). Dislocations in uniform motion on slip or climb planes having periodic force laws. *Mathematical theory of dislocations*, 178–202.

Xiong, L., J. Rigelesaiyin, X. Chen, S. Xu, D. L. McDowell, and Y. Chen (2016). Coarse-grained elastodynamics of fast moving dislocations. *Acta Materialia 104*, 143 – 155.

Yanilkin, A., V. Krasnikov, A. Y. Kuksin, and A. Mayer (2014). Dynamics and kinetics of dislocations in al and al–cu alloy under dynamic loading.

International Journal of Plasticity 55, 94–107.

Youssef, G., R. Crum, S. Prikhodko, D. Seif, G. Po, N. Ghoniem, S. Kodambaka, and V. Gupta (2013). The influence of laser-induced nanosecond rise-time stress waves on the microstructure and surface chemical activity of single crystal cu nanopillars. *Journal of applied physics 113*(8), 084309.